Joint modelling in advanced thin-walled beam models

Hansen, Anders B.; Jönsson, Jeppe; Vieira, Ricardo F.

Published in:
Thin-Walled Structures

Link to article, DOI:
10.1016/j.tws.2021.108798

Publication date:
2022

Document Version
Publisher's PDF, also known as Version of record

Thin-Walled Structures 171 (2022) 108798

Contents lists available at ScienceDirect

Thin-Walled Structures

journal homepage: www.elsevier.com/locate/tws

Full length article

Joint modelling in advanced thin-walled beam models

Anders B. Hansen [a], Jeppe Jönsson [b,*], Ricardo F. Vieira [c]

[a] NIRAS A/S, Sortemosevej 19, DK-3450 Allerød, Denmark
[b] Technical University of Denmark, Department of Civil Engineering, Brovej Building 118, DK-2800 Kgs. Lyngby, Denmark
[c] CERIS, Instituto Superior Técnico, Universidade de Lisboa, Av. Rovisco Pais, 1049-001 Lisbon, Portugal

ARTICLE INFO

Keywords:
Joint modelling
Steel frames
Interface mode reduction
Thin-walled structures

ABSTRACT

A methodology for thin-walled frame analysis using displacement modes of beams at joint interfaces has recently been proposed. This paper introduces an implementation that uses a specific advanced beam element based on semi-analytical beam mode solutions of a generalised beam theory. The end cross-sections of the beam elements consist of wall elements with displacement degrees of freedom that can be joined to conventional finite shell element models of the joints. However, before joining the beam element and joint model at the interface, both beam and joint model are transformed into cross-section displacement mode degrees of freedom. This transformation enables the use of a reduced mode space at the interface as well as in the beam. The quadratic nature of the beam mode equations of the beam element leads to a non-unique number of beam displacement modes. However, this paper introduces an exact mode selection technique that leads to a unique set of modes. Necessary details of the beam element formulation are included in order to make a self-contained description of the mode selection technique. Mode reduction through a length scale dependent choice of the number of exponentially decaying distortional modes is investigated and discussed for three types of joint design in four examples. The three joint design types investigated are based on in-plane membrane action, flexural out-of-plane action and a combination of both membrane and flexural action.

1. Introduction

The analysis of frame structures using beam elements is standard practice. The connections between elements at joints are modelled based on simplifying hypotheses concerning joint rigidity. Commonly, hinges or direct transfer of beam displacements are used without considering the effects of possible relative displacements. Analysing thin-walled frames in this fashion may lead to erroneous results since local torsional and distortional effects are prone to occur. Effects such as cross-sectional distortion are not included in traditional beam elements, and the commonly assumed joint assumptions may also lead to non-economical, oversized or incorrect designs.

This paper utilises a three-dimensional advanced beam element with multiple nodes at each end. The beam ends are connected directly to nodes at joints without constraint equations, and the joints are modelled using standard finite shell elements. Since the advanced beam elements only have nodes at each end, they model the prismatic beam with much fewer degrees of freedom compared to the application of shell elements. Furthermore, by using interface mode reduction, the beams can be reduced to beam elements with even fewer degrees of freedom or even to standard six or seven degrees of freedom beam elements.

Increased focus on steel consumption and use of cold-formed thin-gauge steel challenges the conventional beam design methods that rely on cross-sections keeping their shape. By using interface mode reduction, the examples of this paper show that using standard beam elements can lead to significant displacement errors.

The current work aims at developing advanced beam elements and joining methods that allow an intuitive understanding of modes, interfaces, length scales and mode reduction. This will allow engineers to use advanced frame models in which they can easily adjust the accuracy (number of d.o.f) in zones of interest. The accuracy is controlled by adjusting the locally included number of interface modes without remodelling or modelling the whole structure or specific parts using finite shell elements. Adjusting the number of modes will also allow convergence analysis.

An overview of historical developments and a proposal of a methodology has recently been given by the authors in the paper [1]. The specific implementation of the method used in the following is based on the displacement modes of the thin-walled beam model introduced in [2] and on the thin-walled beam element formulation given in [3]. The selection of unique interface modes is introduced and described in detail in the current paper. This selection is necessary since the beam displacement solutions have an excess number of complex interacting

* Corresponding author.
E-mail address: jej@byg.dtu.dk (J. Jönsson).

https://doi.org/10.1016/j.tws.2021.108798
Received 18 May 2021; Received in revised form 1 November 2021; Accepted 5 December 2021
Available online xxxx

cross-sectional displacement modes along the axial direction of the beam element. Furthermore, the complexity of assembling non-aligned beam elements is taken care of by introducing a three-dimensional finite element joint model. The joint model is an assembly of finite shell elements. This assembly can be adapted to complex geometries and hence ensures that it includes the relevant mechanical behaviour.

An advantage of the method is that the use of beam displacement modes at interfaces allows a reduction in degrees of freedom (d.o.f.) in the numerical model of a frame structure. The mode-based formulation is seen as a potential tool for analyses of thin-walled frame structures. The current paper examines the influence and possibilities of interface mode reduction for different joint designs.

Among thin-walled beam analysis methods that rely on displacement mode formulations is the *Generalised Beam Theory* (GBT) [4,5] which is a well established and efficient approach for analysis of the individual thin-walled beam. An example of the vast development of this method can be seen in the paper by Abambres et al. [6]. Within the framework of GBT, Basaglia, Camotim and Silvestre have developed a method for analysis of thin-walled frame structures, see [7–11]. This method retains the use of a single joint node and is efficient for many standard steel joints. Constraint equations are used to model the compatibility between end section distortional warping and wall transverse bending displacements of the connected beams. As described by Basaglia et al. many joints can be treated based on flange or web continuity through the joint. However, in un-stiffened joints, the transverse bending stiffness in relation to a joint may have to be neglected or estimated. The method cannot easily be used for complicated joints between more general cross-sections.

The idea of joining generalised thin-walled beam elements to a finite shell element joint model has recently not only been pursued by the authors but also by Bianco [12] in his PhD dissertation and by Manta, Gonçalves & Camotim [13]. The approaches are related but differ in methods of approach.

Bianco [12] uses a master–slave node approach to couple advanced GBT elements to shell elements at tubular joints. As the current paper, the GBT elements use the exact longitudinal solution functions. Multi d.o.f. constraints couple shell and GBT elements, with the GBT cross-section nodes as master nodes. The GBT cross-section discretisation contains less d.o.f. compared to the shell element nodes at the interface. Therefore, the constraint transformation matrix is formed using the GBT's sum of modal displacements to express the shell nodal displacements. The shell elements are constrained to have compatible nodal displacements at the interface. Bianco does not investigate interface mode reduction even though it may also be applied in the formulation; (however, one could claim it is implicit in the GBT cross-section discretisation).

Manta et al. [13] use Lagrange multipliers to enforce compatibility of directional nodal displacements (at linked nodes) at interfaces. However, since only the mid-surface nodal displacements of linked nodes are constrained and not the rotations, the procedure loses compatibility across the interface between GBT and shell elements, especially when some nodes are not linked. By extending the macro-element joint zone, the effect of the incompatibility is minimised. This approach is used effectively for linear analysis and buckling analysis with extended shell element zones. Conventional GBT elements based on cubic Hermite interpolation in the axial direction are used, and several of these elements are needed to model a thin-walled member. In [14], [15], the approach is extended to include plastic analysis with adaptive mesh refinement. In this extension, the incompatibility at the interface has to be minimised to avoid stress concentrations at the interface. In [16] the approach is furthermore also extended to include vibration and dynamic analysis with accurate time–history results when compared to shell finite element results.

In contrast to the coupling methods of Bianco and Manta et al. the current paper directly matches the nodal d.o.f. at the joint interface. This means that constraint equations are not used to obtain compatibility. However, full compatibility is not achieved since the membrane part of the triangular shell element in the joint has artificial out of plane rotational d.o.f. Membrane compatibility at a beam to shell interface is only achieved in the limit as the element size is reduced (by refined discretisation) whereas the flexural plate bending part of the shell element is compatible and C1 continuous.

In the presented formulation, the transformation of nodal d.o.f. into beam displacement mode d.o.f. at the interfaces allows the use of interface mode reduction. The possibility of systematic interface mode reduction is investigated using relatively simple illustrative linear elastic examples.

The method presented does not need a considerable extension of the super-element joint zone since it allows short length scale (plate bending) modes to be retained systematically. Retaining short length scale modes is at the cost of an increased number of d.o.f. However, only one GBT element is needed to model a member between joints (at least for linear elastic deformation analysis).

The analysis presented in this paper is performed as a first-order linear elastic deformation analysis assuming isotropic material behaviour and infinitesimal displacements without second-order effects. The methodology presented enables the use of entirely arbitrary joint configurations. For simplicity, the current formulation considers only direct connections representing welded connections, not including other methods such as bolting or screwing. The frame is subdivided into beam elements and joint models.

Besides introducing the specific implementation and the mode selection technique, the current paper aims to investigate joint modelling in advanced beam models and the influence of interface mode reduction. Therefore the focus of the examples is on simple frames with a single joint. The displacement of a well-chosen key point or a few key points is enough to investigate the influence of interface mode reduction and the modelling techniques since the key point displacements result from integrated deformations through the joint. The key point deformations are validated by finite element analysis.

2. The mode-based methodology

A simple introduction to the proposed methodology is given in this section to provide relatively self-contained explanations as we get into details of the specific implementation.

2.1. General beam element formulation

In general, the methodology depends on the use of advanced beam elements, which rely on the determination of cross-sectional displacement modes. Such advanced beam elements have, for example, been developed by Vieira et al. [17,18], and very similarly by Hansen et al. in [2,3]. GBT elements [5] based on simple interpolation functions may also be used in this context. Compared to conventional one-dimensional beam elements with only six to seven d.o.f. at the two end nodes, the advanced beam element formulations have wall elements with several multiple d.o.f. nodes at the end cross-sections. Therefore, the advanced beam elements allow the transfer of torsion and several distortional modes with related warping displacement fields. The methodology is based on the existence of a transformation from beam displacement modes to nodal displacement d.o.f. at the nodes of each end cross-section. This transformation is used at the joint interface and may be performed with a reduced set of modes. The stiffness formulation of the equilibrium equations of the advanced beam element can be formulated in conventional d.o.f.-format as:

$$\mathbf{K}^{\mathrm{B}}\,\mathbf{u}^{\mathrm{B}} = \mathbf{f}^{\mathrm{B}} \tag{1}$$

in which $\mathbf{K}^{\mathrm{B}}$, $\mathbf{u}^{\mathrm{B}}$ and $\mathbf{f}^{\mathrm{B}}$ are the beam stiffness matrix, the beam nodal displacement vector and the beam nodal load vector, respectively. The superscript B is introduced to specify terms related to beam elements. The superscript may also be followed by a number that refers to a specific beam element number. With respect to the displacement vector,

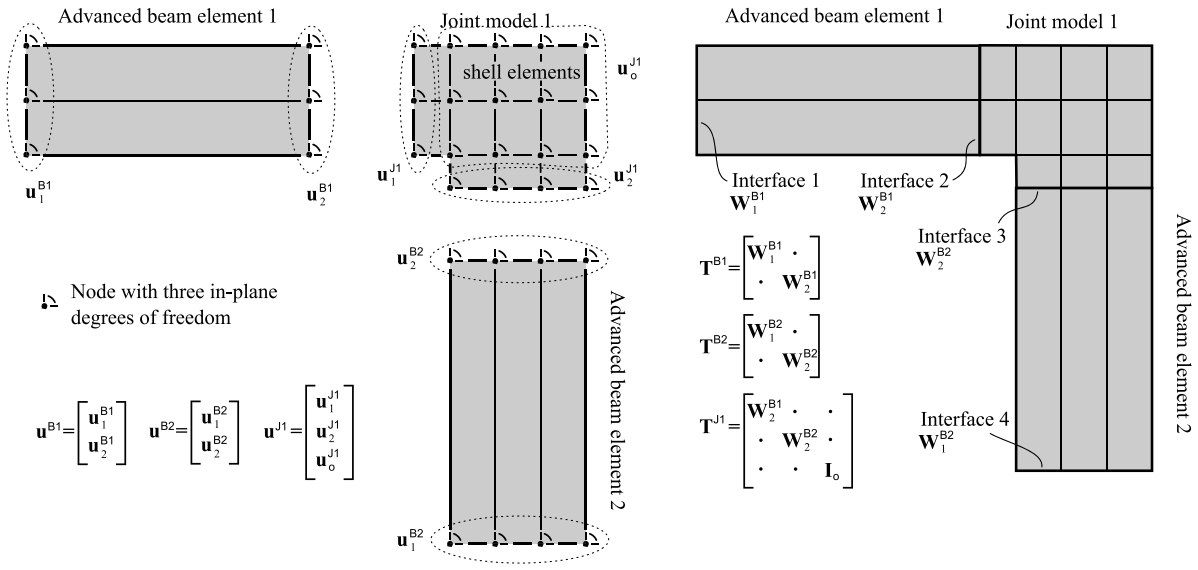

(a) Individual elements and the clustering of the d.o.f..

(b) Assembly of individual elements and interfaces

Fig. 1. Illustration of the assembly of beam elements and joint model at joint interfaces.

it contains a number of conventional d.o.f. based on a discretisation of the cross-section using generic finite wall elements and therefore, $\mathbf{u}^{\mathrm{B}}$ is a column vector with more than two times six d.o.f., dependent on the meshing of the cross-section. The vector components are organised such that the d.o.f. at each beam end are grouped and written as:

$$\mathbf{u}^{\mathrm{B}} = \begin{bmatrix} \mathbf{u}^{\mathrm{B}}_1 \\ \mathbf{u}^{\mathrm{B}}_2 \end{bmatrix} \tag{2}$$

in which $\mathbf{u}^{\mathrm{B}}_1$ and $\mathbf{u}^{\mathrm{B}}_2$ relates to all the nodal displacements at each beam-end cross-section, respectively. A similar separation follows for the load vector $\mathbf{f}^{\mathrm{B}}$. For clarity, a simple two-dimensional example is shown in Fig. 1(a). This example only considers in-plane d.o.f. and thus, for the Advanced beam element 1, $\mathbf{u}^{\mathrm{B1}}_1$ and $\mathbf{u}^{\mathrm{B1}}_2$ contains nine d.o.f. each. The associated beam element stiffness matrix $\mathbf{K}^{\mathrm{B1}}$ is then an 18×18 matrix.

2.2. General formulation of a joint model

Besides the formulations of an advanced mode-based beam element, this methodology introduces a finite element model of the joint. The joint model is a three-dimensional super-element resulting from a meshing of the joint geometry by finite elements. These elements could, for example, be square or triangular shell elements. Based on the standard finite element method, a linear elastic equation system for the joint model can be written as:

$$\mathbf{K}^{\mathrm{J}}\,\mathbf{u}^{\mathrm{J}} = \mathbf{f}^{\mathrm{J}} \tag{3}$$

in which $\mathbf{K}^{\mathrm{J}}$, $\mathbf{u}^{\mathrm{J}}$ and $\mathbf{f}^{\mathrm{J}}$ are the joint stiffness matrix, the joint displacement vector and the joint load vector, respectively. The superscript J refers to joint model. Similar to the beam element notation, the superscript may be followed by a number referring to a global joint model number.

It follows that an interface between an advanced beam element and a joint model must contain the same number of conventional d.o.f., and hence, the d.o.f. in $\mathbf{u}^{\mathrm{J}}$ is organised such that the d.o.f. in each beam-to-joint interface are clustered individually. Therefore, the displacement vector of the joint model $\mathbf{u}^{\mathrm{J}}$ in Eq. (3) can explicitly be written as:

$$\mathbf{u}^{\mathrm{J}} = \begin{bmatrix} \mathbf{u}^{\mathrm{J}}_1 \\ \vdots \\ \mathbf{u}^{\mathrm{J}}_i \\ \vdots \\ \mathbf{u}^{\mathrm{J}}_{n_{\mathrm{I}}} \\ \hline \mathbf{u}^{\mathrm{J}}_{\mathrm{o}} \end{bmatrix} \tag{4}$$

where $\mathbf{u}^{\mathrm{J}}$ without a subscript contains all d.o.f. related to a single joint model whereas each subvector; $\mathbf{u}^{\mathrm{J}}_i$ relates to an interface, for $i = 1, \ldots, n_{\mathrm{I}}$ where n_{I} is the total number of interfaces, i.e. the number of adjacent beam elements. The remaining d.o.f., which are internal d.o.f. not related to any interface, are contained in $\mathbf{u}^{\mathrm{J}}_{\mathrm{o}}$. The assembly in Eq. (4) is illustrated, for a joint model, in the simplified two-dimensional example in the upper hand right corner of Fig. 1(a). Here, $\mathbf{u}^{\mathrm{J1}}_1$ contains nine components, $\mathbf{u}^{\mathrm{J1}}_2$ contains twelve d.o.f., and $\mathbf{u}^{\mathrm{J1}}_{\mathrm{o}}$ contains 36 d.o.f. Therefore, $\mathbf{u}^{\mathrm{J1}}$ is a column vector of 57 components. Separate joint interfaces cannot have nodes in common.

2.3. Transformation and base change at interfaces

The presented approach requires that the interface between a beam element and a joint model share the same number and location of nodes since the d.o.f. must be the same.

The idea is that the d.o.f. at the interfaces shall be expressed in terms of linear independent cross-section displacement modes of the beam. Therefore, a base change is introduced from conventional nodal d.o.f. into cross-sectional beam displacement mode-related d.o.f. These mode-related d.o.f. represent the entire or a reduced set of beam displacement modes. The difference between the conventional and the modal d.o.f. is exemplified in Fig. 2. At each interface, the link between conventional d.o.f., in either beam element or joint model, is established by introducing and using the transformation:

$$\mathbf{u}_i = \mathbf{W}_i\,\boldsymbol{\varphi}_i \tag{5}$$

where the displacement vector $\mathbf{u}_i$ can either be $\mathbf{u}^{\mathrm{B}}_1$ or $\mathbf{u}^{\mathrm{B}}_2$ from Eq. (2), or one of the vectors $\mathbf{u}^{\mathrm{J}}_i$ from Eq. (4) containing conventional nodal d.o.f. related to the nodes at an interface. Accordingly, the columns in the

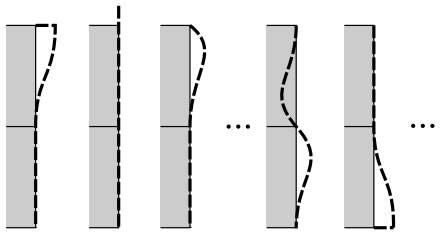

(a) Displacement fields of the beam end in terms of conventional d.o.f.

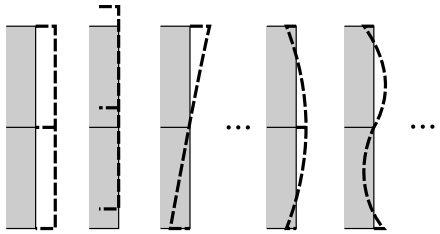

(b) Illustration of interface modes as the modal d.o.f.

Fig. 2. Visualisation of displacement fields related to the conventional d.o.f. and modal d.o.f. at the right end of the Advanced Beam Element 1 in Fig. 1(a).

transformation matrix $\mathbf{W}_i$ contain linear independent cross-sectional displacement modes expressed in terms of conventional d.o.f. These modes will be referred to as interface modes. The last term is the column vector: $\boldsymbol{\varphi}_i$, which contains the individual intensities of the interface modes given in $\mathbf{W}_i$. In fact, the components in the vector $\boldsymbol{\varphi}_i$ are the new modal d.o.f.

Note that the modes chosen in this transformation matrix are governed by the beam element connected to the particular interface. Furthermore, an advantage of the methodology is that the number of interface modes in $\mathbf{W}_i$ can be reduced such that the number of modal d.o.f. is less than the number of conventional d.o.f.

At each interface, the transformation in Eq. (5) shall be applied, meaning that a beam element, which has two interfaces, has two transformations related to its two interfaces – one at each beam end – and thus, the entire beam element transformation and transformation matrix will be written as:

$$\mathbf{u}^{\mathrm{B}} = \mathbf{T}^{\mathrm{B}}\,\boldsymbol{\varphi}^{\mathrm{B}} \quad \text{with } \mathbf{T}^{\mathrm{B}} = \begin{bmatrix} \mathbf{W}_1^{\mathrm{B}} & \cdot \\ \cdot & \mathbf{W}_2^{\mathrm{B}} \end{bmatrix} \tag{6}$$

in which $\mathbf{W}_1^{\mathrm{B}}$ and $\mathbf{W}_2^{\mathrm{B}}$ contain sets of cross-sectional displacement modes chosen to represent the possible displacement fields of the particular interface at each beam-end, respectively. A single dot in a matrix represents a suitable zero-matrix.

An example of the beam element transformation matrix and its two matrices containing the interface modes are shown in Fig. 1(b). Furthermore, Fig. 2(b) presents the interface modes with respect to the advanced beam element 1 from Fig. 1. In the example, these interface modes from Fig. 2(b) are represented as columns in $\mathbf{W}_2^{\mathrm{B1}}$, which occur at Interface 2 according to Fig. 1(b). Similar cross-sectional displacement fields will occur in the transformation matrix $\mathbf{W}_1^{\mathrm{B1}}$.

Applying the transformations described above in Eq. (6) to the advanced beam equation system (2) leads to the following full or reduced number of beam element equilibrium equations:

$$\widetilde{\mathbf{K}}^{\mathrm{B}}\,\boldsymbol{\varphi}^{\mathrm{B}} = \tilde{\mathbf{f}}^{\mathrm{B}} \tag{7}$$

in which the new stiffness matrix is given as $\widetilde{\mathbf{K}}^{\mathrm{B}} = \mathbf{T}^{\mathrm{B}\mathsf{T}}\mathbf{K}^{\mathrm{B}}\,\mathbf{T}^{\mathrm{B}}$ and the load new vector as $\tilde{\mathbf{f}}^{\mathrm{B}} = \mathbf{T}^{\mathrm{B}\mathsf{T}}\mathbf{f}^{\mathrm{B}}$. Once we know the modal displacements $\boldsymbol{\varphi}^{\mathrm{B}}$ we can calculate all internal, displacements, strains and stresses within the beam.

With respect to a joint model, the number of interfaces, and thereby the size of the transformation matrix needed, depends on the number of adjacent beam elements. In accordance with Eqs. (4) and (5) the transformation and the transformation matrix for a joint model will be:

$$\mathbf{u}^{\mathrm{J}} = \mathbf{T}^{\mathrm{J}}\,\boldsymbol{\varphi}^{\mathrm{J}} \tag{8}$$

$$\text{with } \mathbf{T}^{\mathrm{J}} = \left[\begin{array}{ccc:c} \mathbf{W}_1 & & & \\ & \ddots & & \\ & & \mathbf{W}_{n_{\mathrm{I}}} & \\ \hdashline & & & \mathbf{I}_{\mathrm{o}} \end{array}\right] \text{ and } \boldsymbol{\varphi}^{\mathrm{J}} = \left[\begin{array}{c} \boldsymbol{\varphi}_1^{\mathrm{J}} \\ \vdots \\ \boldsymbol{\varphi}_{n_{\mathrm{I}}}^{\mathrm{J}} \\ \hdashline \mathbf{u}_{\mathrm{o}}^{\mathrm{J}} \end{array}\right]$$

Herein, $\mathbf{I}_{\mathrm{o}}$ is an identity matrix with a size equal to the number of internal d.o.f. in the joint model – meaning those d.o.f. that are not located at an interface. Each set of interface modes contained in the matrices $\mathbf{W}_i$ for $i = 1, \ldots, n_{\mathrm{I}}$ may differ in number and size depending on the number of nodes at each specific interface as well as the number of interface modes to be included in the transformation. However, a beam element and a joint model sharing the same interface must use the same interface modes as well as the same number of modes. For example, in Fig. 1(b), the matrix $\mathbf{W}_2^{\mathrm{B1}}$ is used both in the beam element transformation matrix $\mathbf{T}^{\mathrm{B1}}$ as well as in the joint model transformation matrix $\mathbf{T}^{\mathrm{J1}}$. For clarity, it has been illustrated in Fig. 1(b) how the different transformation matrices are composed. Note also that nodes are not shared between interfaces. Applying the transformations described above, in Eq. (8), to the joint equation system in Eq. (3) leads to the following (possibly reduced) joint model equilibrium equation system:

$$\widetilde{\mathbf{K}}^{\mathrm{J}}\,\boldsymbol{\varphi}^{\mathrm{J}} = \tilde{\mathbf{f}}^{\mathrm{J}} \tag{9}$$

Herein, the modal joint stiffness matrix is found as $\widetilde{\mathbf{K}}^{\mathrm{J}} = \mathbf{T}^{\mathrm{J}\mathsf{T}}\mathbf{K}^{\mathrm{J}}\,\mathbf{T}^{\mathrm{J}}$, and the load vector as $\tilde{\mathbf{f}}^{\mathrm{J}} = \mathbf{T}^{\mathrm{J}\mathsf{T}}\mathbf{f}^{\mathrm{J}}$. Once we know the modal displacements $\boldsymbol{\varphi}^{\mathrm{J}}$, we can calculate the related conventional nodal displacements at the interfaces of the joint using the transformation Eq. (8). When using a reduced number of modes we assuming that the neglected interface displacement modes are zero. Thereby, all internal, displacements, strains and stresses within the joint can be calculated.

2.4. Full frame system

The entire equilibrium equation system for a frame can be assembled from the modal equation systems of members and joints. The assembly results in the linear equation system:

$$\mathbf{K}^{\mathrm{sys}}\,\boldsymbol{\varphi}^{\mathrm{sys}} = \mathbf{f}^{\mathrm{sys}} \tag{10}$$

in which the system d.o.f. are given by $\boldsymbol{\varphi}^{\mathrm{sys}}$ corresponding to displacement mode intensities at the interfaces.

This introduction to the mode-based methodology will first be followed by a brief description of the joint model implementation. Secondly, the advanced thin-walled beam element formulation with its complex displacement modes will be described, and thirdly the new selection of interface modes will be introduced.

3. Joint model implementation

In the current work, the finite element model of the joint is kept simple by using plane triangular shell elements having three nodes and six d.o.f. at each node, see Fig. 3. The shell element combines a plane constant strain triangle (CST) element and a triangular plane flexural element.

The CST-element is implemented with extra so-called drilling d.o.f. corresponding to rotation vectors normal to the plate. The artificial stiffness of this rotational d.o.f. is defined as a fraction of the largest value in the element stiffness matrix diagonal. The d.o.f. related to membrane actions are denoted by a w-subscript. For further reference,

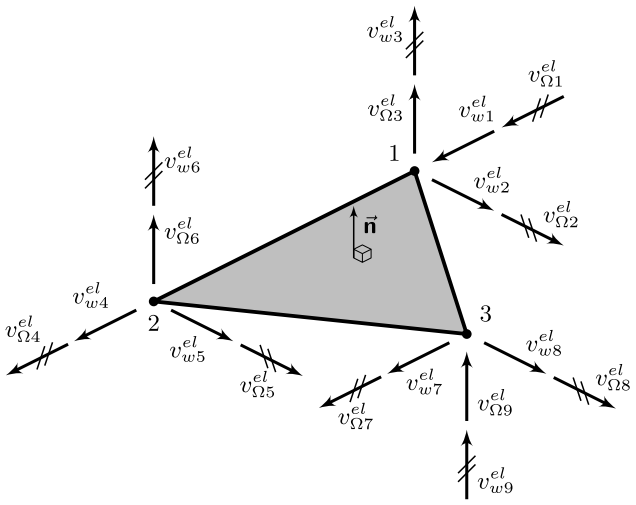

Fig. 3. Triangular finite shell element and its d.o.f.

see Cook et al. [19] where a detailed description of the CST-element is given.

The triangular plane flexural element used is the Specht-element, [20]. This element covers the flexural displacements, and an Ω-subscript denotes the related d.o.f.

For a given element discretisation of the joint an entire joint model stiffness matrix, $\mathbf{K}^{\mathrm{J}}$, with corresponding boundary and load vectors, $\mathbf{u}^{\mathrm{J}}$ and $\mathbf{f}^{\mathrm{J}}$, respectively, can be assembled leading to the linear equation system in Eq. (3). The conventional nodal d.o.f. given in $\mathbf{u}^{\mathrm{J}}$ can be divided into three categories:

- $\mathbf{u}_{\mathrm{j}}$ D.o.f. that are shared between joint and beam at connected interfaces. Hence, according to Eq. (4) we have: $\mathbf{u}_{\mathrm{j}}^{\mathsf{T}} = \left[\, \mathbf{u}_{1}^{\mathrm{J}\,\mathsf{T}},\ \cdots,\ \mathbf{u}_{n_{\mathrm{I}}}^{\mathrm{J}\,\mathsf{T}} \,\right]$.
- $\mathbf{u}_{\mathrm{f}}$ Joint model d.o.f. selected for boundary conditions or loading. These must be included and remain accessible in the joint model as part of $\mathbf{u}^{\mathrm{J}}_{\mathrm{o}}$ in Eq. (4).
- $\mathbf{u}_{\mathrm{i}}$ Internal d.o.f., that represent all the remaining d.o.f. not covered by either $\mathbf{u}_{\mathrm{j}}$ or $\mathbf{u}_{\mathrm{f}}$. The d.o.f. in $\mathbf{u}_{\mathrm{i}}$ will along with $\mathbf{u}_{\mathrm{f}}$ also be a part of $\mathbf{u}^{\mathrm{J}}_{\mathrm{o}}$ in Eq. (4). These d.o.f. may be eliminated by condensation.

Having rearranged the system in Eq. (3), based on the three categories of d.o.f. listed above, we may write the joint equilibrium equations as follows:

$$\left[\begin{array}{cc:c} \mathbf{K}_{\mathrm{jj}} & \mathbf{K}_{\mathrm{jf}} & \mathbf{K}_{\mathrm{ji}} \\ \mathbf{K}_{\mathrm{fj}} & \mathbf{K}_{\mathrm{ff}} & \mathbf{K}_{\mathrm{fi}} \\ \hdashline \mathbf{K}_{\mathrm{ij}} & \mathbf{K}_{\mathrm{if}} & \mathbf{K}_{\mathrm{ii}} \end{array}\right] \left[\begin{array}{c} \mathbf{u}_{\mathrm{j}} \\ \mathbf{u}_{\mathrm{f}} \\ \hdashline \mathbf{u}_{\mathrm{i}} \end{array}\right] = \left[\begin{array}{c} \mathbf{f}_{\mathrm{j}} \\ \mathbf{f}_{\mathrm{f}} \\ \hdashline \mathbf{f}_{\mathrm{i}} \end{array}\right] \tag{11}$$

The internal d.o.f. located in the vector $\mathbf{u}_{\mathrm{i}}$ can be eliminated such that:

$$\mathbf{u}_{\mathrm{i}} = \left[\, \mathbf{K}_{\mathrm{ii}} \,\right]^{-1} \left(\mathbf{f}_{\mathrm{i}} - \left[\, \mathbf{K}_{\mathrm{ij}} \;\; \mathbf{K}_{\mathrm{if}} \,\right] \left[\begin{array}{c} \mathbf{u}_{\mathrm{j}} \\ \mathbf{u}_{\mathrm{f}} \end{array}\right] \right) \tag{12}$$

and thus, the equation system is rewritten into:

$$\tilde{\mathbf{K}}^{\mathrm{J}}\, \tilde{\mathbf{u}}^{\mathrm{J}} \;=\; \tilde{\mathbf{f}}^{\mathrm{J}} \tag{13}$$

where the stiffness matrix is computed according to Eq. (14) and the boundary and load vectors follow in Eq. (15).

$$\tilde{\mathbf{K}}^{\mathrm{J}} = \left[\begin{array}{cc} \mathbf{K}_{\mathrm{jj}} & \mathbf{K}_{\mathrm{jf}} \\ \mathbf{K}_{\mathrm{fj}} & \mathbf{K}_{\mathrm{ff}} \end{array}\right] - \left[\begin{array}{c} \mathbf{K}_{\mathrm{ji}} \\ \mathbf{K}_{\mathrm{fi}} \end{array}\right] \left[\, \mathbf{K}_{\mathrm{ii}} \,\right]^{-1} \left[\, \mathbf{K}_{\mathrm{ij}} \;\; \mathbf{K}_{\mathrm{if}} \,\right] \tag{14}$$

$$\tilde{\mathbf{u}}^{\mathrm{J}} = \left[\begin{array}{c} \mathbf{u}_{\mathrm{j}} \\ \mathbf{u}_{\mathrm{f}} \end{array}\right] \quad \text{and} \quad \tilde{\mathbf{f}}^{\mathrm{J}} = \left[\begin{array}{c} \mathbf{f}_{\mathrm{j}} \\ \mathbf{f}_{\mathrm{f}} \end{array}\right] - \left[\begin{array}{c} \mathbf{K}_{\mathrm{ji}} \\ \mathbf{K}_{\mathrm{fi}} \end{array}\right] \left[\, \mathbf{K}_{\mathrm{ii}} \,\right]^{-1} \mathbf{f}_{\mathrm{i}} \tag{15}$$

After the elimination of internal d.o.f., the remaining ones are listed such that we have the d.o.f. at beam interfaces followed by those d.o.f. at the boundaries and the loaded ones. Hence, the non-condensed d.o.f. from Eq. (15) are explicitly written as:

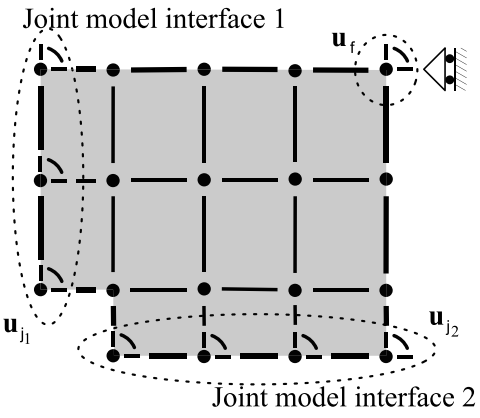

Fig. 4. Simplified two-dimensional joint model with d.o.f. according to Eq. (16).

$$\tilde{\mathbf{u}}^{\mathrm{J}} = \left[\begin{array}{c} \mathbf{u}_{\mathrm{j}} \\ \hdashline \mathbf{u}_{\mathrm{f}} \end{array}\right] = \left[\begin{array}{c} \mathbf{u}_{\mathrm{j}_1} \\ \vdots \\ \mathbf{u}_{\mathrm{j}_i} \\ \vdots \\ \mathbf{u}_{\mathrm{j}_{n_{\mathrm{I}}}} \\ \hdashline \mathbf{u}_{\mathrm{f}} \end{array}\right] \tag{16}$$

where a vector $\mathbf{u}_{\mathrm{j}_i}$ having an additional subscript is a subset of $\mathbf{u}_{\mathrm{j}}$. Each subset contains all the conventional finite element d.o.f. at the beam-to-joint interface i. The total number of interfaces in a specific joint model is denoted n_{I}. For illustration purpose, Fig. 4 shows the two-dimensional joint model from Fig. 1(a) where the notation introduced in Eq. (16) is applied.

4. Advanced beam implementation

The advanced beam element and thin-walled beam theory that is applied in this study has been presented by Hansen and Jönsson in [2,3]. As mentioned, to address and give improved explanations of the specific implementation and especially to explain the selection of interface modes, the formulation of the advanced beam theory and element will be addressed in some detail in this section.

4.1. Kinematic assumptions and beam equations

An advanced thin-walled beam, including the beam and wall coordinate systems, is illustrated in Fig. 5. The cross-section is modelled using straight wall elements of constant thickness. An example of a cross-sectional wall element is shown in Fig. 6. The division of the cross-section into smaller elements is adopted to enhance approximation features. The wall element supports both flexural and membrane behaviours and is governed by six nodal d.o.f. at each end.

The displacement of a single wall element is defined from the plate element centre surface in its three local coordinate directions, $\boldsymbol{u} = [u_n \;\; u_s \;\; u_z]^{\mathsf{T}}$. For each wall element these are independently approximated through interpolation functions along the coordinate s. The interpolation functions are governed by the nodal displacement components at the wall element ends as the d.o.f.-vectors $\mathbf{u}^{el}_{w}(z)$ and $\mathbf{u}^{el}_{\Omega}(z)$, which relates to in-plane (index w) and out-of-plane (index Ω) translations and rotations as illustrated in Fig. 6. The d.o.f. in the vectors $\mathbf{u}^{el}_{w}(z)$ and $\mathbf{u}^{el}_{\Omega}(z)$ are sums of m displacement modes and can be computed as:

$$\begin{aligned} \mathbf{u}^{el}_{w}(z) &= \sum_{i=1}^{m} \mathbf{v}^{el\,i}_{w}\; \psi^{i}(z)\, c_i \\ \mathbf{u}^{el}_{\Omega}(z) &= \sum_{i=1}^{m} \mathbf{v}^{el\,i}_{\Omega}\; \eta^{i}(z)\, c_i \end{aligned} \tag{17}$$

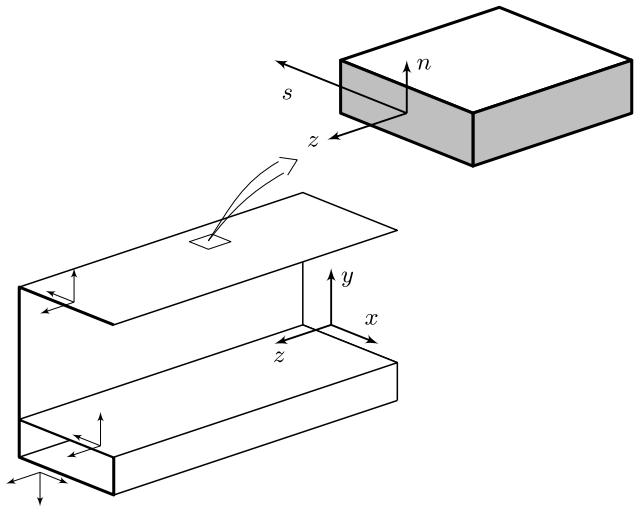

Fig. 5. Cartesian beam coordinate system (x, y, z) and local cross-sectional coordinate systems (n, s, z) of a thin-walled beam member.

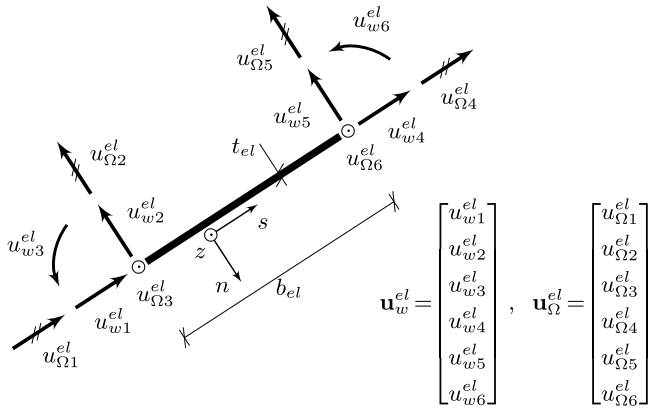

Fig. 6. Wall element, which is used to discretise the cross-section also illustrating the displacement components from $\mathbf{u}^{el}_w$ and $\mathbf{u}^{el}_\Omega$, respectively.

in which $\mathbf{v}^{el^i}_w$ and $\mathbf{v}^{el^i}_\Omega$ are wall element mode displacement vectors, $\psi^i(z)$ and $\eta^i(z)$ are the axial amplitude functions, and c_i is a mode intensity factor (mode d.o.f.) used to scale the intensity of each displacement mode. Accordingly, the displacements of a single wall element are approximated as follows:

$$\begin{aligned} u_n(s,z) &= \mathbf{N}_n(s)\,\mathbf{u}^{el}_w(z) \\ u_s(n,s,z) &= \left[\ \mathbf{N}_s(s) - n\,\mathbf{N}_{n,s}(s)\ \right]\mathbf{u}^{el}_w(z) \\ u_z(n,s,z) &= \left[\ \mathbf{N}_\Omega(s) + n\,\mathbf{N}_\alpha(s)\ \right]\mathbf{u}^{el}_\Omega(z) \end{aligned} \tag{18}$$

The interpolation vectors $\mathbf{N}_n$ and $\mathbf{N}_\alpha$ contain linear Lagrange interpolation functions, and the vectors $\mathbf{N}_s$ and $\mathbf{N}_\Omega$ includes cubic Hermite interpolation functions, see also ref. [21]. Regarding the notation, an n or s-index that follows a comma indicates a derivative, e.g.: $(\cdot)_{,s} = d(\cdot)/ds$, whereas axial derivatives are denoted by using the Lagrange notation, i.e. a prime: $(\cdot)' = d(\cdot)/dz$.

In this particular theory, displacements are obtained under the small displacement hypothesis, and thus, the strains are obtained as:

$$\boldsymbol{\varepsilon} = \boldsymbol{\mathcal{S}}\,\boldsymbol{u} \quad \text{with } \boldsymbol{\varepsilon} = [\ \varepsilon_{ss}\ ,\ \varepsilon_{zz}\ ,\ \gamma_{sz}\ ,\ \gamma_{nz}\ ]^\mathsf{T} \tag{19}$$

$$\boldsymbol{\mathcal{S}} = \begin{bmatrix} 0 & \frac{\partial}{\partial s} & 0 \\ 0 & 0 & \frac{\partial}{\partial z} \\ 0 & \frac{\partial}{\partial z} & \frac{\partial}{\partial s} \\ \frac{\partial}{\partial z} & 0 & \frac{\partial}{\partial n} \end{bmatrix} \tag{20}$$

The stresses are formulated on the assumption of linear elastic isotropic material properties, and the non-null stress field is found from the constitutive relation:

$$\boldsymbol{\sigma} = \boldsymbol{D}\,\boldsymbol{\varepsilon} \tag{21}$$

in which the non-null stress components are written in the vector format: $\boldsymbol{\sigma} = [\ \sigma_{ss}\ ,\ \sigma_{zz}\ ,\ \tau_{sz}\ ,\ \tau_{nz}\ ]^\mathsf{T}$. The elastic constitutive matrix $\boldsymbol{D}$ is defined for a plane stress state, taking into account the Poisson effect as follows:

$$\boldsymbol{D} = \begin{bmatrix} E_s & \nu E_s & 0 & 0 \\ \nu E_s & E_s & 0 & 0 \\ 0 & 0 & G & 0 \\ 0 & 0 & 0 & G \end{bmatrix} \tag{22}$$

Here, E_s is the plate type elastic modulus: $E_s = E/(1-\nu^2)$, where E is the modulus of elasticity; ν is the Poisson coefficient; and G is the shear modulus: $G = E/(2(1+\nu))$.

Equilibrium for the beam element is found using the linear elastic strain energy, derived by integrating the strain energy density over the entire continuum V. Hence, in its purest form, the strain energy is expressed as:

$$U = \frac{1}{2}\int_V \boldsymbol{\varepsilon}^\mathsf{T}\boldsymbol{D}\,\boldsymbol{\varepsilon}\,dV \tag{23}$$

The volume integral is separated into an integration over the beam length ℓ along z, and an integration over each wall element thickness t_{el} and wall element width b_{el} being supplemented by an assembly of wall elements. Hence, substituting Eq. (18) into the strain formulation, in Eq. (19), and evaluating the strain energy of Eq. (23) leads to the local wall element stiffness matrices given in Table 1. By assembling the wall elements based on standard transformations and their d.o.f., the strain energy from Eq. (23) is rewritten into the following expression based on stiffness matrices and displacement vectors.

$$U = \frac{1}{2}\int_0^\ell \begin{bmatrix} \mathbf{u}_w \\ \mathbf{u}_\Omega \\ \mathbf{u}'_w \\ \mathbf{u}'_\Omega \end{bmatrix}^\mathsf{T} \begin{bmatrix} \mathbf{K}^s_{ww} & \cdot & \cdot & \mathbf{K}^{s\sigma}_{w\Omega} \\ \cdot & \mathbf{K}^\gamma_{\Omega\Omega} & \mathbf{K}^\gamma_{\Omega w} & \cdot \\ \cdot & \mathbf{K}^\gamma_{w\Omega} & \mathbf{K}^\gamma_{ww} & \cdot \\ \mathbf{K}^{\sigma s}_{\Omega w} & \cdot & \cdot & \mathbf{K}^\sigma_{\Omega\Omega} \end{bmatrix} \begin{bmatrix} \mathbf{u}_w \\ \mathbf{u}_\Omega \\ \mathbf{u}'_w \\ \mathbf{u}'_\Omega \end{bmatrix} dz \tag{24}$$

The superscripts s, σ, and γ on the stiffness matrices identifies terms related to transverse, axial and shear strains, respectively.

A system of second-order beam differential equilibrium equations is deduced from the strain energy in Eq. (24). This is done by requiring the strain energy to be stationary using the principle of variation, introducing kinematical admissible virtual displacement fields and performing partial integration of selected terms. This results in a homogeneous system of coupled second-order differential equations, i.e. beam equilibrium equations expressed in terms of displacement vectors, as follows:

$$\mathbf{K}_2\mathbf{u}''(z) + \mathbf{K}_1\mathbf{u}'(z) + \mathbf{K}_0\mathbf{u}(z) = \mathbf{0} \tag{25}$$

where the matrices $\mathbf{K}_0$, $\mathbf{K}_1$ and $\mathbf{K}_2$ are defined as blocks of cross-sectional stiffness matrices and the common displacement vector $\mathbf{u}(z)$ is introduced containing both the translational and warping displacement vectors. To clarify the terms in Eq. (25) they can be written as:

$$\begin{aligned} \mathbf{K}_0 &= \begin{bmatrix} \mathbf{K}^s_{ww} & \cdot \\ \cdot & -\mathbf{K}^\gamma_{\Omega\Omega} \end{bmatrix}, \quad \mathbf{K}_2 = \begin{bmatrix} -\mathbf{K}^\gamma_{ww} & \cdot \\ \cdot & \mathbf{K}^\sigma_{\Omega\Omega} \end{bmatrix}, \\ \mathbf{K}_1 &= \begin{bmatrix} \cdot & \mathbf{K}^{s\sigma}_{w\Omega} - \mathbf{K}^\gamma_{w\Omega} \\ \mathbf{K}^{\sigma s}_{\Omega w} - \mathbf{K}^\gamma_{\Omega w} & \cdot \end{bmatrix}, \quad \mathbf{u}(z) = \begin{bmatrix} \mathbf{u}_w(z) \\ \mathbf{u}_\Omega(z) \end{bmatrix} \end{aligned} \tag{26}$$

Each block matrix is $n \times n$, where n is six times the number of nodes within a discretised beam cross-section.

Table 1
Local stiffness matrices of a wall-element.

Stiffness matrices related to normal stresses	Stiffness matrices related to shearing stresses
$\mathbf{k}^{s}_{ww} = \int_0^{b_{el}} \left(t_{el} E_s \mathbf{N}^{\mathsf{T}}_{s,s} \mathbf{N}_{s,s} + \frac{t^3_{el}}{12} E_s \mathbf{N}^{\mathsf{T}}_{n,ss} \mathbf{N}_{n,ss} \right) ds$	$\mathbf{k}^{\gamma}_{ww} = \int_0^{b_{el}} \left(t_{el} G \mathbf{N}^{\mathsf{T}}_{n} \mathbf{N}_{n} + t_{el} G \mathbf{N}^{\mathsf{T}}_{s} \mathbf{N}_{s} + \frac{t^3_{el}}{12} G \mathbf{N}^{\mathsf{T}}_{n,s} \mathbf{N}_{n,s} \right) ds$
$\mathbf{k}^{\sigma}_{\Omega\Omega} = \int_0^{b_{el}} \left(t_{el} E_s \mathbf{N}^{\mathsf{T}}_{\Omega} \mathbf{N}_{\Omega} + \frac{t^3_{el}}{12} E_s \mathbf{N}^{\mathsf{T}}_{\alpha} \mathbf{N}_{\alpha} \right) ds$	$\mathbf{k}^{\gamma}_{\Omega\Omega} = \int_0^{b_{el}} \left(t_{el} G \mathbf{N}^{\mathsf{T}}_{\alpha} \mathbf{N}_{\alpha} + t_{el} G \mathbf{N}^{\mathsf{T}}_{\Omega,s} \mathbf{N}_{\Omega,s} + \frac{t^3_{el}}{12} G \mathbf{N}^{\mathsf{T}}_{\alpha,s} \mathbf{N}_{\alpha,s} \right) ds$
$\mathbf{k}^{s\sigma}_{w\Omega} = \int_0^{b_{el}} \left(t_{el} \nu E_s \mathbf{N}^{\mathsf{T}}_{s,s} \mathbf{N}_{\Omega} - \frac{t^3_{el}}{12} \nu E_s \mathbf{N}^{\mathsf{T}}_{n,ss} \mathbf{N}_{\alpha} \right) ds$	$\mathbf{k}^{\gamma}_{w\Omega} = \int_0^{b_{el}} \left(t_{el} G \mathbf{N}^{\mathsf{T}}_{n} \mathbf{N}_{\alpha} + t_{el} G \mathbf{N}^{\mathsf{T}}_{s} \mathbf{N}_{\Omega,s} - \frac{t^3_{el}}{12} G \mathbf{N}^{\mathsf{T}}_{n,s} \mathbf{N}_{\alpha,s} \right) ds$
$\mathbf{k}^{\sigma s}_{\Omega w} = \int_0^{b_{el}} \left(t_{el} \nu E_s \mathbf{N}^{\mathsf{T}}_{\Omega} \mathbf{N}_{s,s} - \frac{t^3_{el}}{12} \nu E_s \mathbf{N}^{\mathsf{T}}_{\alpha} \mathbf{N}_{n,ss} \right) ds$	$\mathbf{k}^{\gamma}_{\Omega w} = \int_0^{b_{el}} \left(t_{el} G \mathbf{N}^{\mathsf{T}}_{\alpha} \mathbf{N}_{n} + t_{el} G \mathbf{N}^{\mathsf{T}}_{\Omega,s} \mathbf{N}_{s} - \frac{t^3_{el}}{12} G \mathbf{N}^{\mathsf{T}}_{\alpha,s} \mathbf{N}_{n,s} \right) ds$

4.2. Beam solution modes

Solutions to the differential equation system given in Eq. (25) are found by substituting an exponential solution function into the amplitude functions of $\mathbf{u}(z)$, i.e. $\psi(z) = \eta(z) = e^{\lambda z}$ in Eq. (17). With this substitution, the differential equation system turns into a polynomial eigenvalue problem. The non-trivial solutions will have an exponential decay pattern along the beam axis governed by the inverse length scale parameter λ. This parameter is deduced as the eigenvalue, and the cross-sectional displacement fields are given as the corresponding eigenvectors in the polynomial eigenvalue problem.

The solutions to the polynomial eigenvalue problem correspond to those with a non-null eigenvalue and those with a null-eigenvalue. For null eigenvalues, the amplitude function is expressed as a polynomial function instead of the exponential one. This solution space will reflect the twelve fundamental beam modes according to paper [2] whereas the solutions with non-null eigenvalues reflect the exponential beam modes (higher-order beam modes).

4.2.1. Fundamental beam modes

The solutions having eigenvalues equal to zero represents the fundamental beam modes. These modes can be described by polynomial amplitude functions that are limited to third-order. Since these modes share the same eigenvalue, it follows that since the algebraic and geometric multiplicity of the eigenvalues do not coincide, some generalised eigenvectors are related to these solutions as well, Strang [22]. This was solved by Vieira [23] and by Morandini et al. [24] using a Jordan Chain method extracting additional cross-section solution fields. These solution fields extended the twelve eigenvectors with associated null-eigenvalues into four sets of twelve cross-sectional displacement fields. However, the engineering-based procedure outlined by Hansen & Jönsson [2] is implemented in the current work. Hence, the fundamental beam modes are found by substituting a polynomial solution function into the equilibrium equation, i.e. Eq. (25). Such a polynomial solution can for solution mode j be written as:

$$\mathbf{u}_{p_j}(z) = \left(\frac{z^3}{3!}\mathbf{v}_{3j} + \frac{z^2}{2!}\mathbf{v}_{2j} + z\mathbf{v}_{1j} + \mathbf{v}_{0j} \right) c_{p_j} \tag{27}$$

For the polynomial solution of third-order, a single displacement mode is a combination of up to four cross-sectional displacement fields given in the vectors $\mathbf{v}_0$, $\mathbf{v}_1$, $\mathbf{v}_2$, and $\mathbf{v}_3$, being coefficients in the polynomial function. The cross-sectional displacement fields for all twelve fundamental modes are contained in the matrix $\mathbf{V}_p$ as:

$$\mathbf{V}_p = \begin{bmatrix} \mathbf{V}_3 & \mathbf{V}_2 & \mathbf{V}_1 & \mathbf{V}_0 \end{bmatrix} \tag{28}$$

Each matrix, $\mathbf{V}_0$ to $\mathbf{V}_3$ contains twelve column vectors being the eigenvectors. Accordingly, the j-subscript, in Eq. (27), indicates a column index in $\mathbf{V}_i$ for $i = 0, \ldots, 3$ and $j = 1, \ldots, 12$. The c_{p_j} is a constant that determines the intensity of each mode and is stored in its own column vector $\mathbf{c}_p$. Now, the polynomial part of the solution to Eq. (25) is conveniently written as:

$$\mathbf{u}_p(z) = \mathbf{V}_p \, \boldsymbol{\Psi}_p(z) \, \mathbf{T}_p \, \mathbf{c}_p \tag{29}$$

where $\mathbf{V}_p$ is given in Eq. (28) and the remaining components are:

$$\boldsymbol{\Psi}_p(z) = \begin{bmatrix} \frac{z^3}{6}\mathbf{I}_p & \cdot & \cdot & \cdot \\ \cdot & \frac{z^2}{2}\mathbf{I}_p & \cdot & \cdot \\ \cdot & \cdot & z\mathbf{I}_p & \cdot \\ \cdot & \cdot & \cdot & \mathbf{I}_p \end{bmatrix}, \; \mathbf{T}_p = \begin{bmatrix} \mathbf{I}_p \\ \mathbf{I}_p \\ \mathbf{I}_p \\ \mathbf{I}_p \end{bmatrix}, \; \mathbf{c}_p = \begin{bmatrix} c_{p_1} \\ c_{p_2} \\ \vdots \\ c_{p_{n_z}} \end{bmatrix} \tag{30}$$

in which $\mathbf{I}_p$ is an identity matrix of size $n_z \times n_z$.

Examples of the cross-sectional displacement fields given in $\mathbf{V}_p$ are illustrated in Fig. 7. These cross-sectional displacement fields are deduced with respect to the cross-section assessed in Example 1, Section 6.1.

4.2.2. Exponential beam modes

The polynomial eigenvalue problem found by substituting the amplitude functions with exponential functions is rewritten into a generalised eigenvalue problem according to Tisseur & Meerbergen [25] by introducing a state-vector notation. The exponential solutions to Eq. (25) are deduced as cross-sectional displacement fields corresponding to eigenvectors with exponential amplitude functions. Therefore, the cross-sectional displacement field has a decay pattern along the beam axis dependent on its corresponding eigenvalue.

The eigenvectors with non-null eigenvalues are sorted in ascending order and stored as column vectors in a matrix $\mathbf{V}_e$. The associated eigenvalues are substituted into exponential functions in the diagonal of the amplitude matrix $\boldsymbol{\Psi}_e(z)$ as:

$$\boldsymbol{\Psi}_e(z) = \begin{bmatrix} e^{\lambda_1 z} & & & \\ & e^{\lambda_i z} & & \\ & & \ddots & \\ & & & e^{\lambda_{n_e} z} \end{bmatrix} \tag{31}$$

where λ_i is the eigenvalue to solution mode i and n_e is the number of exponential solution modes. The eigenvalues correspond to inverse length scales. Therefore, the eigenvalues are organised in ascending order corresponding to decreasing length scales of the solution functions.

The exponential part of the solution space of Eq. (25) can be written as:

$$\mathbf{u}_e(z) = \mathbf{V}_e \, \boldsymbol{\Psi}_e(z) \, \mathbf{I}_e \, \mathbf{c}_e \tag{32}$$

In which, $\mathbf{I}_e$ is a "dummy" unit matrix of size $n_e \times n_e$ and has been introduced to ease the summation with fundamental beam modes. The mode intensity constants are stored in $\mathbf{c}_e$ as:

$$\mathbf{c}_e = \begin{bmatrix} c_{e_1} & c_{e_2} & \ldots & c_{e_{n_e}} \end{bmatrix}^{\mathsf{T}} \tag{33}$$

Examples of exponential cross-sectional displacement fields are given in Fig. 8. As for the fundamental beam modes, these modes are deduced for the cross-section assessed in Example 1, Section 6.1.

4.2.3. Complete displacement formulation

The full homogeneous solution space of the beam equilibrium equation system (25) corresponds to a summation of the displacement formulations in Eqs. (29) and (32). These we add together and obtain a full homogeneous solution space expressed in terms of beam displacement modes being:

$$\mathbf{u}(z) = \mathbf{u}_p(z) + \mathbf{u}_e(z)$$

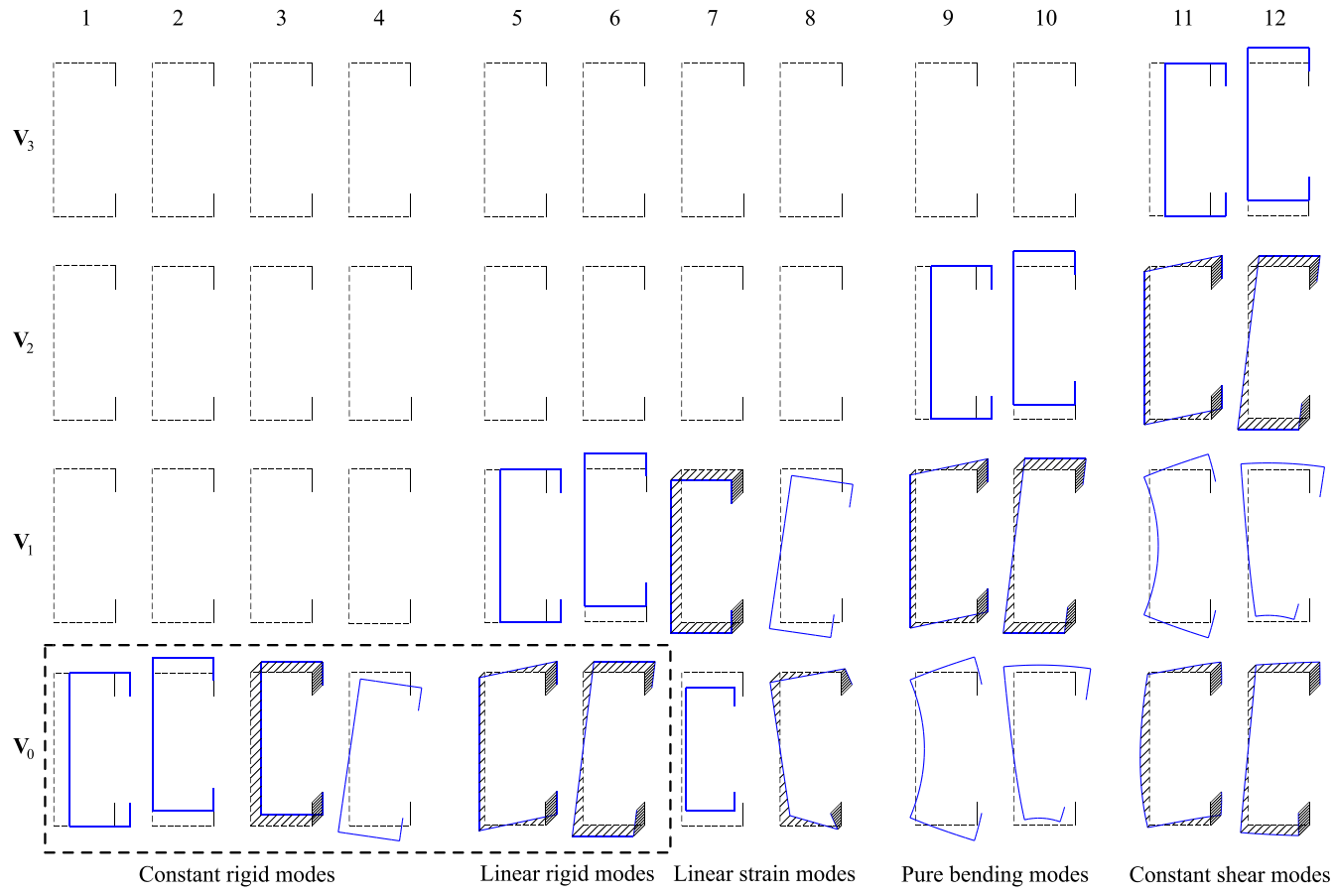

Fig. 7. Cross-sectional displacement modes used to represent the fundamental beam displacement modes, which have the polynomial amplitude function. Each row represents the content in the four matrices $\mathbf{V}_3$ to $\mathbf{V}_0$, respectively. The dashed-line-box highlights the six rigid motions adopted as part of the interface modes.

$$= \begin{bmatrix}\mathbf{V}_p & \mathbf{V}_e\end{bmatrix} \begin{bmatrix}\boldsymbol{\Psi}_p(z) & \cdot \\ \cdot & \boldsymbol{\Psi}_e(z)\end{bmatrix} \begin{bmatrix}\mathbf{T}_p & \cdot \\ \cdot & \mathbf{I}_e\end{bmatrix} \begin{bmatrix}\mathbf{c}_p \\ \mathbf{c}_e\end{bmatrix}$$

$$= \mathbf{V}\ \boldsymbol{\Psi}(z)\ \mathbf{T}_c\ \mathbf{c} \tag{34}$$

in which the individual components are defined throughout the previous two subsections, 4.2.1 and 4.2.2.

4.3. Beam stiffness matrix and equation system

Using the formulation of the beam displacement modes of Eq. (34) we are able to integrate the strain energy in Eq. (24) using the full set of modes. Remembering that the definition of the cross-section displacement vector $\mathbf{u}(z)$ is given in Eq. (26). The integration of the strain energy using Hadamard and Kronecker products is described in the paper [3] and results in:

$$U = \tfrac{1}{2}\ \mathbf{c}^{\mathsf{T}}\ \mathbf{K}_{\mathrm{c}}\ \mathbf{c} \tag{35}$$

Using Eq. (34) we have a direct relation between the end displacements $\mathbf{u}^{\mathrm{B}}$ of a beam element and the intensity constants given as:

$$\mathbf{u}^{\mathrm{B}} = \begin{bmatrix}\mathbf{u}(0) \\ \mathbf{u}(\ell)\end{bmatrix} = \mathbf{A}\mathbf{c} \quad \text{where } \mathbf{A} = \begin{bmatrix}\mathbf{V}\ \boldsymbol{\Psi}(0)\ \mathbf{T}_c \\ \mathbf{V}\ \boldsymbol{\Psi}(\ell)\ \mathbf{T}_c\end{bmatrix} \tag{36}$$

The transformation matrix $\mathbf{A}$ is a square, positive definite and invertible matrix. Thus, the strain energy is rewritten into conventional finite element format with conventional displacements as:

$$U = \tfrac{1}{2}\ \mathbf{u}^{\mathrm{B}\mathsf{T}}\ \mathbf{K}^{\mathrm{B}}\ \mathbf{u}^{\mathrm{B}} \tag{37}$$

in which the beam stiffness matrix is given by:

$$\mathbf{K}^{\mathrm{B}} = \left[\mathbf{A}^{-1}\right]^{\mathsf{T}}\ \mathbf{K}_{\mathrm{c}}\ \mathbf{A}^{-1} \tag{38}$$

This enables us to write the beam finite element equation system in accordance with Eq. (1) as:

$$\mathbf{K}^{\mathrm{B}}\ \mathbf{u}^{\mathrm{B}} = \mathbf{f}^{\mathrm{B}} \tag{39}$$

in which $\mathbf{f}^{\mathrm{B}}$ is the element load vector related to the d.o.f. of both end cross-sections of the beam.

As seen in this section, the advanced beam element used has spacial solution modes consisting of interacting cross-section displacement modes; therefore, it is necessary to carefully select cross-sectional displacement modes that are directly related to these spacial modes. Due to the mode-based approach in the advanced beam element, it is possible to choose (cross-section) interface modes directly related to the length scale of the modes. The reason for formulating the full stiffness matrix is to enable a modal reduction based on the (cross-section) interface modes, which are directly related to the ordered spacial modes of the advanced beam element. Other advanced beam formulations will also need to establish the complete transformation from mode space to conventional displacement space. However, the transformation is easier to establish because these formulations are based directly on the cross-section mode space and the independent interpolation between the end cross-sections.

5. Selection of interface modes

The mode-based methodology outlined in Section 2 uses beam cross-sectional displacement fields to formulate the transformation between conventional d.o.f. and modal d.o.f. Because the transformation is applied at the beam end cross-sections, only the cross-sectional displacement fields at the specific endpoints are of interest.

The beam mode determination procedure is an exact solution method for the second-order beam differential equation system, which

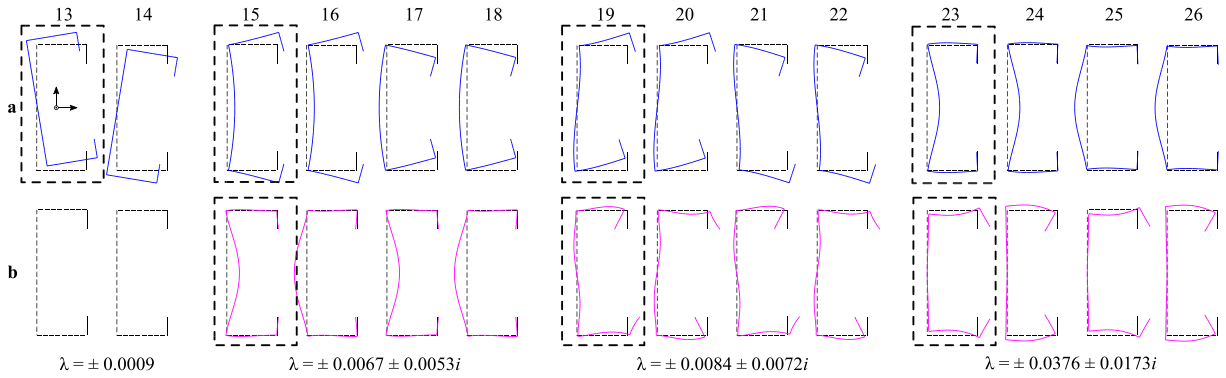

(a) The in-plane part of cross-sectional displacement fields separated into the real and imaginary part. The upper row represents the real part and the lower row represents the imaginary part

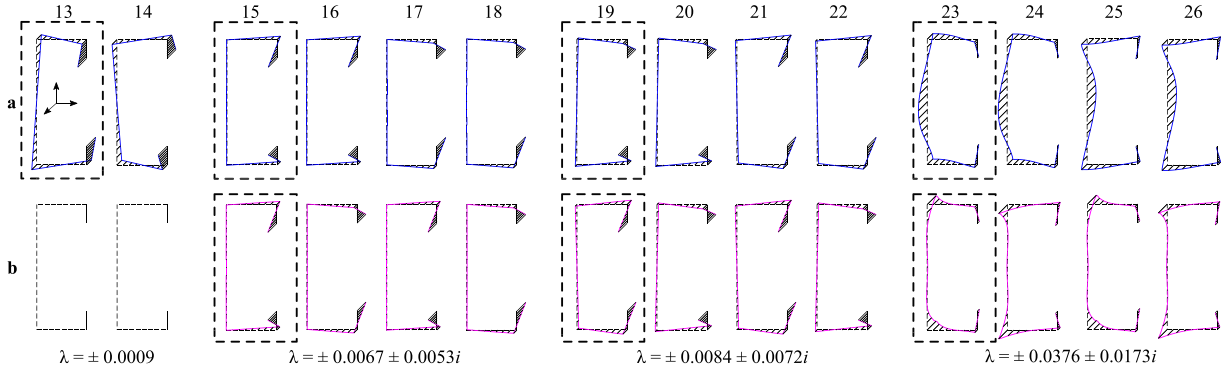

(b) The out-of-plane part of the cross-sectional displacement fields (warping). The upper row represents the real part of the mode and the lower row represents the imaginary part

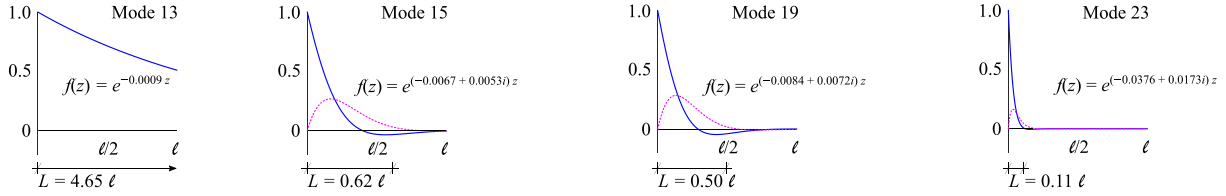

(c) Examples of the exponential amplitude functions illustrated for each of the four different eigenvalues. In this illustration $\ell = 750$mm. The continuous blue curve represents the real part and the dashed magenta curve represents the imaginary part

Fig. 8. The first number of cross-sectional displacement fields from $\mathbf{V}_e$ are illustrated in (a) and (b), which have an exponential axial variation illustrated in (c). The modes are represented by one pair of real modes (mode 13–14) and three quadruples of complex modes (mode 15–18, 19–22, and 23–26). In each of the two subfigures (a) and (b), a column represents a cross-sectional displacement field $\mathbf{v} = \pm\mathbf{a} \pm \mathbf{b}i$ that has been separated into the real part of the mode (vector **a**) and the imaginary part of the mode (vector **b**). The dashed boxes indicates the modes that are chosen as interface modes.

is solved as a quadratic eigenvalue problem. However, as a consequence, twice as many solution modes are deduced. Therefore, these modes are not independent modes of the vector-space, which is a requirement in the mode-based methodology presented in Section 2. Hence, a mode selection is required to formulate the unique transformation matrix $\mathbf{W}$ used in Eq. (5).

The cross-sectional beam displacement fields are given as columns in the matrix $\mathbf{V}$ (see also Eq. (34)). The modes both represent solutions with a polynomial axial variation (Fig. 7) as well as solutions with exponential axial variations (Fig. 8). The modes are categorised as fundamental and exponential modes, respectively. Thus, the matrix $\mathbf{V}$ may, therefore, be subdivided into two subsets, which we write as:

$$\mathbf{V} = \left[\mathbf{V}_p \, , \, \mathbf{V}_e \right] \tag{40}$$

In the following two subsections, the selection procedure for each of these mode types is described.

5.1. Selection of fundamental modes

The polynomial modes contained in $\mathbf{V}_p$ consists of four submatrices, $\mathbf{V}_p = [\mathbf{V}_3 \, \mathbf{V}_2 \, \mathbf{V}_1 \, \mathbf{V}_0]$, where each subscript refers to the polynomial order that the specific mode refers to. For clarity see also Eq. (27) and Fig. 7 in which each row represents the content of the four matrices $\mathbf{V}_0$ to $\mathbf{V}_3$, respectively. According to ref. [3] the modes in $\mathbf{V}_1$, $\mathbf{V}_2$ and $\mathbf{V}_3$ can be found as cross-sectional displacement modes already given in $\mathbf{V}_0$, and therefore, the modes in $\mathbf{V}_1$, $\mathbf{V}_2$ and $\mathbf{V}_3$ are not relevant for the procedure finding a set of orthogonal cross-sectional beam displacement fields. Investigating all modes, it can be concluded that only six cross-sectional displacement modes out of twelve should be chosen. Thus, the natural choice is only to use the(first) six rigid cross-sectional displacement modes in $\mathbf{V}_0$ as interface modes in $\mathbf{W}$. These six modes are highlighted in Fig. 7 by the dashed box. The remaining independent six modes in $\mathbf{V}_0$ correspond to distortional behaviours, which are due to Poisson effects and shear stresses. These modes are combinations of the cross-sectional displacement fields in the exponential set of cross-sectional displacement fields contained in $\mathbf{V}_e$ and thus not independent, but at the same time not lost as a part of the solution space.

5.2. Selection of exponential modes

Because the solution modes in $\mathbf{V}_e$ are found as solutions to a quadratic eigenvalue problem, the distortional modes are determined as

either real pairs or complex quadruples. The cross-sectional displacement-vectors are similar only with different signs within each pair of modes or quadrupled set of modes. Therefore, these are not linearly independent.

To avoid repeated modes in the transformation matrix and thereby a singular transformation matrix, the following procedure is implemented to choose the needed modes from the full set of modes in $\mathbf{V}_e$. Accordingly, in case of a real pair of cross-sectional displacement modes we have: $[\mathbf{v} \ \ -\mathbf{v}] \in \mathbf{V}_e$. Here, the first vector is chosen for the transformation, and the other one is rejected (see, for example, mode 13 and 14 in Fig. 8, where mode 13 will be the chosen one and mode 14 will be rejected. As a consequence, mode 13 is a part of the interface modes, which has been illustrated in Fig. 11 as well (as mode 7).

In the case of having a set of complex quadruples, the selection is a bit more sophisticated. A complex set of modes can be written as:

$$[\ \mathbf{v} \quad \bar{\mathbf{v}} \quad -\mathbf{v} \quad -\bar{\mathbf{v}}\ ] \in \mathbf{V}_e \tag{41}$$

where a single mode can be decomposed even further into: $\mathbf{v} = \mathbf{a} + \mathbf{b}i$ with $\mathbf{a}$ and $\mathbf{b}$ representing the real and imaginary part of the vector, respectively. Thus, the four vectors in Eq. (41) can be expressed as different combinations of $\mathbf{a}$ and $\mathbf{b}$. To represent the complex quadruples from Eq. (41) in the transformation matrix, the vectors $\mathbf{a}$ and $\mathbf{b}$ are chosen as the unique modes for the transformation and therefore added separately to the matrix $\mathbf{W}$ (see also Fig. 8, where the modes 15, 19, and 23 are the modes used as interface modes, which have lead to the interface modes 8 to 13 in Fig. 11).

5.3. Check and normalisation of interface modes

It is checked that the chosen interface modes span the full vector-space by conveniently computing the null-space of the mode-transformation-matrix $\mathbf{W}$ (containing the modes column-wise). If the null-space of $\mathbf{W}$ is an empty set, this has been confirmed. The statement may be written as:

$$\mathcal{N}(\mathbf{W}) \in \emptyset \tag{42}$$

where $\mathcal{N}(\ )$ is the null-space operator.

To be able to compare mode intensities when analysing a solution, the modes in $\mathbf{W}$ are normalised by letting the translational d.o.f. with the largest absolute magnitude in each mode be equal to unity. This concerns both in-plane translations as well as translations out of the cross-sectional plane.

5.4. Reduction in the number of interface modes

The mode-transformation-matrix $\mathbf{W}$ does not need to include all exponential modes (as columns in the matrix). The number of modes may be reduced according to length scale of the beam modes by including only modes larger than a certain length scale, i.e. by including a reduced number of modes from the start of the full mode space. The assumption is that the larger the length scale of a mode is, the more important it is for the overall displacement behaviour. However, the joint design significantly influences the number of modes needed since the deformation of the interface depends on the distortional and warping stiffness of the joint itself at the interface. In other words, if the design relies on plate bending and not on the transfer of in-plane forces, it will be necessary to include a high number of modes. This is due to the fact that flexural plate modes have quite small length scales in comparison to large scale distortional modes of the connected beam. It will be addressed further in the example section.

As discussed in the paper by Hansen & Jönsson [3], each higher-order beam mode has an exponential amplitude function, which is described by a decay length factor being the eigenvalue determined in the quadratic eigenvalue problem. The decay length is then given as:

$$L_a = \frac{\epsilon}{Re(\lambda)} \tag{43}$$

where $Re(\lambda)$ is the real part of each eigenvalue associated with each amplitude function and ϵ is a sensitivity factor. In the literature, different values of this sensitivity factor have been argued. Nonetheless, we use $\epsilon = \pi$ due to the geometric interpretation of the modes, Jönsson [26]. A direct illustration of the decay length L_a, for different amplitude functions, is shown in the graphs in Fig. 8(c).

Including modes having decay lengths that are much shorter than the shell element size in the joint does not make sense and is not expected to increase the model accuracy.

6. Examples and interface mode reduction

In thin-walled frame structures, the joints have to handle difficult boundary conditions between members involving polynomial beam modes, the exponential torsional mode as well as distortional modes. At the very least, it is necessary that the torsional warping, i.e. the classic seventh d.o.f. can be modelled adequately in connections between I-beams. However, for cross-sections that have more than three walls, it is necessary to include at least some important distortional warping modes in the modelling. Finally, for some joints, it may be necessary to include local distortional modes related to flexure in the walls of the cross-sections.

The design of joints depends on the required stiffness and the magnitude of section forces that have to be transferred between members of the frame structure. Stiff and strong joints, so-called rigid joints, are often designed utilising force transfer through in-plane membrane action between the walls of member cross-sections and plates of the joint, while minimising flexural plate bending behaviour in the connected parts. Simple, flexible welded joints, like those performed in truss structures between rectangular tubular members of different widths, rely solely on the transfer of section forces through flexural (bending) action in the walls of the connected tubes. In contrast, joints between tubular members of identical width rely on and effectively utilise the transfer of section forces through membrane action in combination with flexural action in the walls of connected tubes.

Different joint design types will be investigated through four academic examples. In these examples, the designs lead to the transfer of forces from cross-section walls to the joint through (a) in-plane membrane action (mainly), (b) flexural out-of-plane action, or (c) a combination of membrane and flexural action.

The first example investigates four joint designs of a portal frame corner for lipped channel sections. Three of these corners rely on (a) in-plane membrane action, whereas one without extra stiffeners relies on (c) a combination of both membrane and flexural action.

The second and third examples involve a beam to column joint between rectangular tubular sections of unequal or equal width, respectively relying on (b) flexural out-of-plane action and (c) a combination of both membrane and flexural action.

The fourth example introduced by Manta et al. [13] investigates a tapered I-section joint. This joint relies on (c) a combination of membrane and flexural actions since it does not include stiffeners.

These academic examples have been chosen as benchmark tests to investigate and illustrate the influence of joint design on interface mode reduction. The influence of not using enough joint interface modes is that the displacement prediction of the frame model becomes inaccurate or even wrong. The influence of the number of joint interface modes will be investigated in the examples by analysing displacements of key points in the structural model. Thus, the examples will focus on displacements, well knowing that the predicted stress fields will be less accurate and depend on the mode types. Stress fields of a model similar to the first example but with other boundary conditions are shown in [1].

The presented approach has been implemented using the numerical software MATLAB [27]. In the implementation of the triangular shell element shown in Fig. 3 the artificial stiffness related to the rotational d.o.f. (v^{el}_{w3}, v^{el}_{w6}, v^{el}_{w9}) has been set to 10^{-9} times the maximum absolute

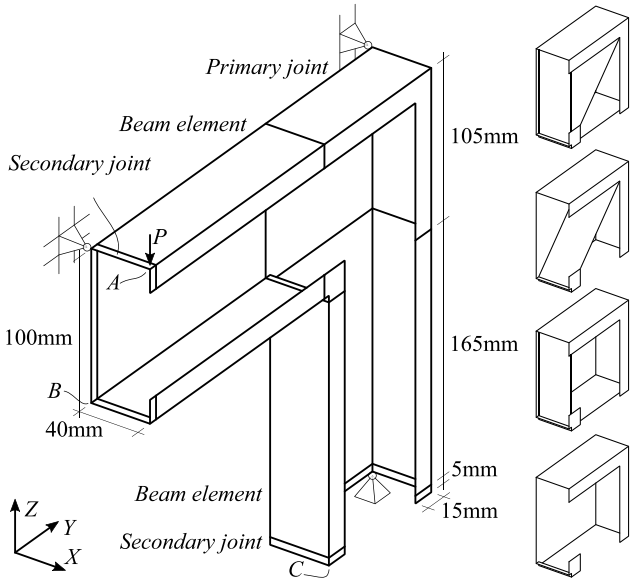

Fig. 9. Portal frame corner. All plates are 2 mm thick, and the point load is $P = 100$ N. The four different primary joint designs are shown to the right.

value in the diagonal of the shell element stiffness matrix. The commercial finite element software Abaqus [28] and its S3 shell element is used to make finite element shell models of the structural examples in order to compare the displacements found at relevant key points. In all examples, the Young's modulus used is $E = 210$ GPa and the Poisson ratio used is $\nu = 0.3$.

6.1. Example 1 – portal frame corners

This example investigates four different joint designs of a rectangular portal frame corner that joins a column and a beam channel section. Three of these joints are designed to transfer section forces through in-plane action in section walls and joint plates. However, the last design depends on a combination of in-plane action in the web and lips and out of plane action in the perpendicularly joined flanges. The lipped channel section, the load and support conditions are purely academic and have been chosen to include both torsional and distortional warping. The example involves a rather small thin-walled cross-section compared to normal practice, and the load magnitude was originally chosen rather small to give the same displacement magnitude as a similar example with alternate boundary conditions given in [1].

Fig. 9 illustrates the orthogonal assembly of the two equal length thin-walled lipped channel sections and shows the four joint designs. The dimensions are given in the figure and the caption text. The frame corner is modelled by two advanced beam elements and three joints. One primary joint at the corner and two secondary joints at the two "free" beam ends. Secondary joints enable conventional nodal boundary conditions instead of applying boundary conditions to beam type interface modes. The boundary conditions are applied to the joints at three individual nodes. The node at the bottom is a fixed simple support (with all rotations free), the node at the corner of the joint is a simple support that is movable in the Z-direction, and finally, the node at the horizontal beam end is a simple support that is movable in the Y- and Z-directions. Thus, the three supports prevent the overall rigid body movements of the frame. The structure is statically determined. The load P is applied as a nodal load with a magnitude of 100 N.

The four different joint configurations used to illustrate the influence of joint stiffener geometry on mode reduction are the following:

[all] A joint fully stiffened by three stiffening plates,
[dia] A joint with a diagonal stiffening plate,

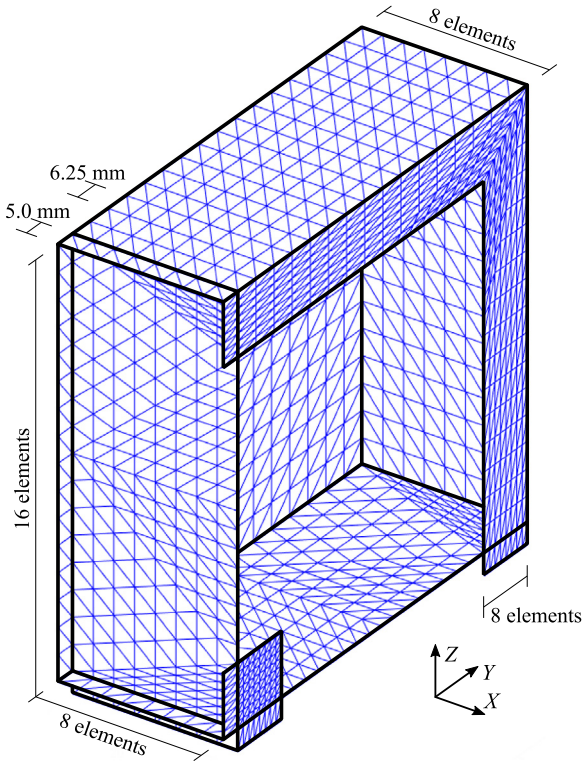

Fig. 10. Mesh density of the primary joint model for the box configuration.

[box] A joint with two (box) stiffening plates,
[non] A joint without any stiffening plates.

These four configurations are shown to the right in Fig. 9. The names in squared parenthesis will be used to reference the specific joint configuration.

The discretisations of the joint models are governed by the cross-section nodes of the connected beam elements. To illustrate the mesh density, Fig. 10 shows a discretised primary joint model with the box stiffeners. The beam element stiffness matrices are deduced using the approach outlined in Section 4 with a discretisation having eight wall elements in each lip, eight wall elements in the flanges, and sixteen wall elements along the web. This results in a total of 294 interface modes, i.e. d.o.f. at each interface. The discretisation of the lip has to enable appropriate modelling of the distortional displacements of the lip. Perhaps it has been chosen to be unnecessarily dense. The first 13 cross-sectional displacement modes used as part of the transformation matrix $\mathbf{W}$ are illustrated in Fig. 11. The order of the modes is based on the eigenvalues that relate to the beam displacement modes (see also Fig. 8). The first six interface modes are the rigid displacements of the interface, then follow the global distortional modes, and finally the local displacement modes. Since the two beam elements are identical, they share the same stiffness matrix as well as the same cross-sectional displacement modes to be used when transforming the formulation into the mode-based formulation.

6.1.1. Ex. 1: Comparison with a finite element shell model

Before turning to the influence of mode reduction, the analysis results for a model using all interface modes are compared to the results of a full finite element shell model. Using `Abaqus`, the portal frames with the four joint designs are meshed using a structured mesh of triangular S3 shell elements with full integration. The maximum element side length of the mesh is approximately 5 mm, and in some regions, an even finer mesh is used.

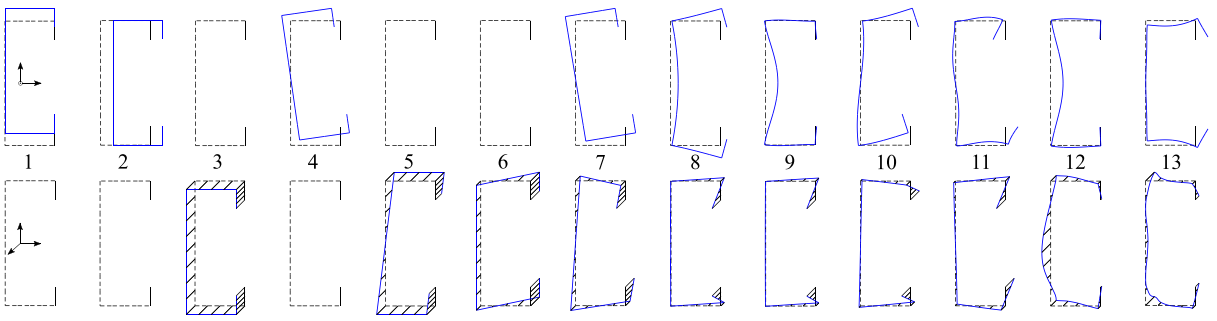

Fig. 11. The first 13 modal-d.o.f. out of 294 modes representing the interface modes. The upper row represents the in-plane part and the lower row represents the displacements orthogonal to the cross-sectional plane (warping).

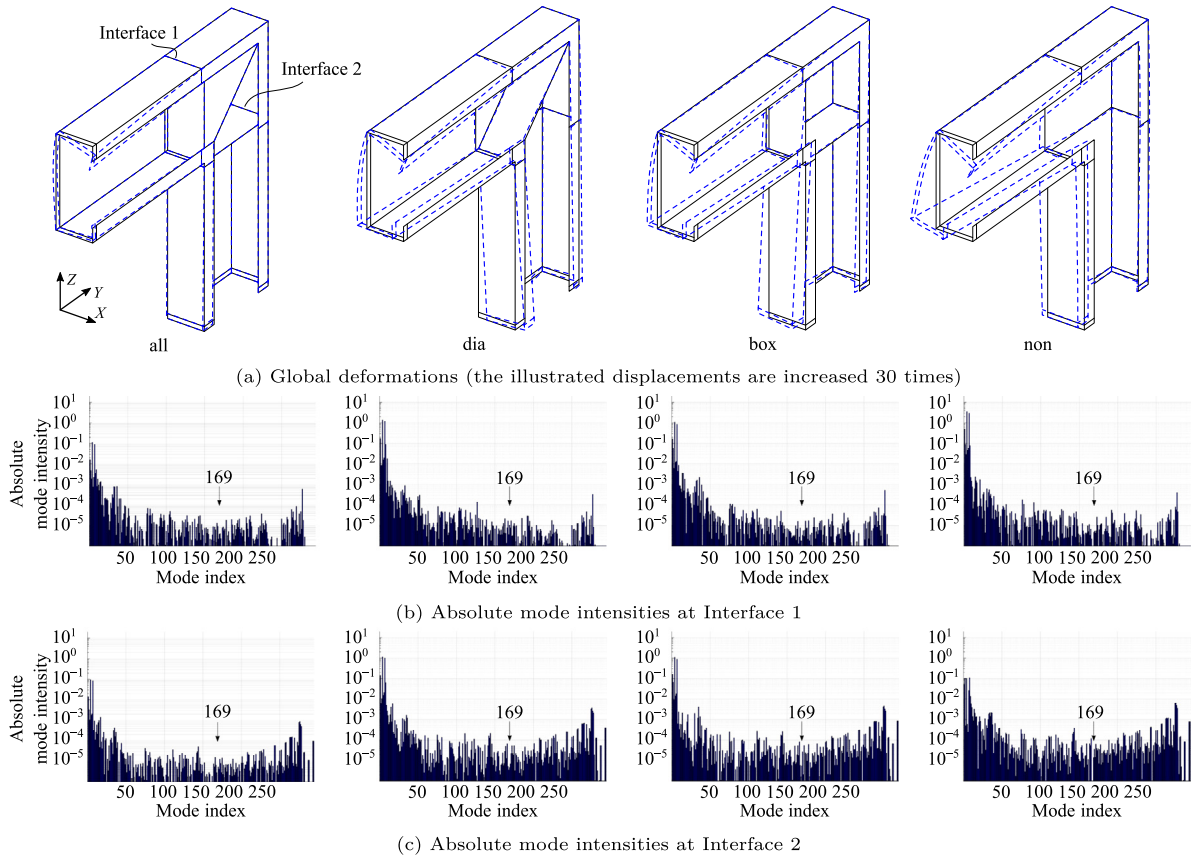

Fig. 12. Global deformation and mode intensities at the two interfaces for the primary joint models.

The main directional displacement at the three key locations A, B, and C, (shown in Fig. 9) have been extracted from the analysis and listed in Table 2 for all four joint configurations. The relative difference of the displacement at these points compared to the Abaqus shell model are given as the Δ-values listed in the table for each joint configuration. For example, for the fully stiffened joint configuration [all] the relative difference between the present model and the finite element shell model is found at point A to be: $\Delta u_Z = 2.2\ \%$, at point B to be: $\Delta u_X = 1.3\ \%$, and at point C to be: $\Delta u_X = 1.4\ \%$. Plots of the frame corner deformations are shown in Fig. 12(a). Furthermore, three-dimensional visualisations of the absolute displacements are shown using colour scales for both present models and Abaqus models in Fig. 13. It can be observed that the models result in practically identical displacement patterns. Note that the colour scales deviate slightly due to different plotting routines used in Matlab and Abaqus. From Table 2 it can be seen that there are some relatively large differences at points B and C in both the case of the box-stiffened and the non-stiffened frame. These are due to differences in the modelling of wall behaviour in advanced beam elements and the triangular S3 shell elements used in the Abaqus to model the members. The rather simple pointwise application of supports and load also induce differences in the two modelling results. However, we have chosen to note and accept these differences in the current work. It does not influence the analysis of mode intensities and interface mode reduction.

6.1.2. Ex. 1: interface mode intensities

The four frame corner joint designs have been analysed using the full modes space. Fig. 12(a) shows the global displacements for each of the four configurations. It is observed that increasing the stiffness by adding stiffeners in the joint reduces the displacements at points A and B at the beam end, but it also changes the displacement field of the column and the displacement at point C. It can also be observed how the transmission of rotation and distortion is increasingly prevented when adding stiffeners to the joint. The intensities of each mode at

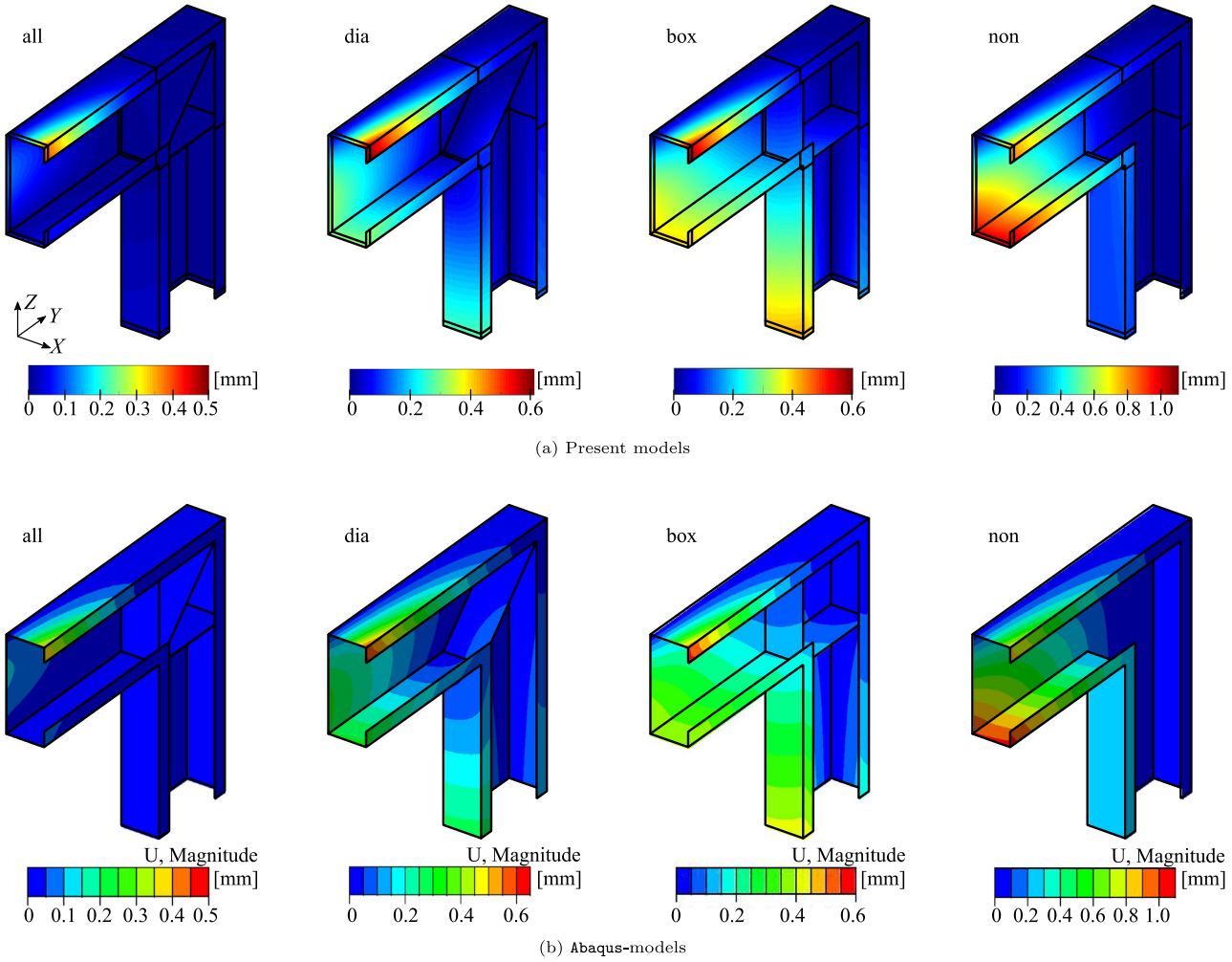

Fig. 13. Total absolute displacements for the portal frame for the joint configurations.

Table 2
Key point displacements of the portal frame models.

Joint design	Key point	Disp. comp	Abaqus [mm]	Present method [mm]	Relative difference Δ
[All]	A	u_Z	−0.386	−0.394	2.1%
	B	u_X	−0.0127	−0.0122	3.9%
	C	u_X	−0.0298	−0.0295	1.0%
[Dia]	A	u_Z	−0.585	−0.586	0.2%
	B	u_X	−0.305	−0.305	0.0%
	C	u_X	0.265	0.264	0.4%
[Box]	A	u_Z	−0.554	−0.542	2.2%
	B	u_X	−0.395	−0.343	13.2%
	C	u_X	−0.413	−0.361	12.6%
[Non]	A	u_Z	−0.816	−0.801	1.8%
	B	u_X	−1.026	−0.990	3.5%
	C	u_X	−0.229	−0.197	14.0%

the interface between a beam element and the primary (corner) joint model are shown in Figs. 12(b) and 12(c) as bar-diagrams. These intensities are directly extracted from $\boldsymbol{\varphi}^{\text{sys}}$ as $\boldsymbol{\varphi}^{\text{J}}$, which in turn can be subdivided into $\boldsymbol{\varphi}^{\text{J}}_1$ and $\boldsymbol{\varphi}^{\text{J}}_2$ at each interface. Each graph relates to one of the two corner joint interfaces. One bar represents a mode, and the intensity is given on the vertical axis. Please note that the vertical axis is logarithmic. Common for all graphs in Fig. 12 is that the modes with the highest intensity, i.e. the most pronounced displacement modes at an interface, are among the first ones. This is the case for all four joint configurations. The graphs indicate that the primary interface modes being activated are those related to the rigid movements of the cross-section (mode 1–6) and the first torsional and distortional displacement fields (mode 7–10). However, it is observed that there are some modes at the end of the spectrum with increasing intensities. This is a tendency observed in all four joint configurations. Investigating the importance and influence of these modes results in the conclusion that the modes contribute only with a small, very localised displacement (at the end of each lip). It is also important to note that the somewhat spurious modes with a high mode index could be neglected since their decay length is very short and even shorter than the finite elements used in the joint model adjacent to the interfaces. In the current example, this means that modes with an index higher than 169 have too small decay lengths at the interface boundary and could be neglected for this reason. This mode index has been indicated in the graphs of Fig. 12).

6.1.3. Ex. 1: Interface mode reduction

The number of interface modes are reduced by eliminating all modes above a certain mode index (i.e. less than a certain decay length) in the interface transformation matrix, i.e. Eq. (6) and (8). Reducing the maximum number of modes from 294 modes to 280 modes, then by twenty modes down to 60 modes and further by ten down to 10 modes and finally to 7 modes allows us to plot the influence of mode reduction as shown in Fig. 14. The figure shows the relative difference compared to the inclusion of all 294 modes for all four joint designs for the main displacements at locations A, B and C. It is seen that nearly no variation is observed for reductions down to 100 modes. This confirms

Table 3
Relative difference in key point displacements for interface mode reduction compared to the use of all 294 modes.

Joint design	Key point	Disp. comp	Disp. all modes [mm]	Number of included interface modes				
				100	50	20	10	7
[All]	A	u_Z	−0.394	0.4%	0.5%	1.0%	7.5%	92%
	B	u_X	−0.0122	0.9%	1.6%	3.1%	46%	328%
	C	u_X	−0.0295	0.4%	0.8%	2.2%	13%	10%
[dia]	A	u_Z	−0.586	0.2%	0.4%	0.9%	6.7%	94%
	B	u_X	−0.305	0.5%	0.9%	3.6%	15%	83%
	C	u_X	0.265	0.3%	0.7%	3.4%	21%	112%
[box]	A	u_Z	−0.542	0.4%	0.6%	1.4%	7.2%	84%
	B	u_X	−0.343	0.4%	0.6%	1.7%	10%	45%
	C	u_X	−0.361	0.4%	0.6%	1.8%	10%	53%
[non]	A	u_Z	−0.801	0.4%	0.6%	1.4%	5.8%	88%
	B	u_X	−0.990	0.9%	1.6%	3.8%	18%	79%
	C	u_X	−0.197	1.2%	1.1%	2.1%	3.9%	3.8%

our hypothesis that the transformation modes with the highest indices relate to modes with very localised effects and do not influence global deformations. Even a reduction below 50 modes can be done without introducing relative differences above 2 % at all three locations (A, B, C) for all four stiffening configurations ([non], [dia], [box] and [all]).

Some of the relative difference values for key points have been assembled in Table 3. As expected, it can be seen that including only seven interface modes leads to significant errors due to the too stiff behaviour of the beam element resembling a classic Vlasov beam element. This shows that transferring only beam modes or the seven d.o.f. of Vlasov theory is not sufficient, [29]. However, it is interesting that by including ten modes in the advanced beam elements (in other words, by including the modes 8 and 10 related distortional displacements of the lips of the channel section shown in Fig. 11), there is a dramatic improvement. It can also be seen that all the four design models of the joint have relative differences of similar magnitudes. The reason being that all designs include the important in-plane transfer of forces in the section. Note that some of the larger relative difference values are based on very small displacement values and are therefore of less importance.

6.2. Example 2 – tubular joint with unequal width sections

This second academic example investigates the effect of interface mode reduction for a connection between a cantilever tubular (RHS) beam and a tubular (RHS) column with clamped ends, as illustrated in Fig. 15. The unequal widths of the rectangular hollow sections mean that plate bending action is invoked to transfer the cantilever beam moment. The model consists of three advanced beam elements, of which two are used for the column part and one for the cantilever beam part. Furthermore, four joints are used. There are secondary joint models at each free beam element end and one primary joint model located where the three beam elements intersect. The geometry and dimensions, as well as load and boundary conditions, are shown in Fig. 15. The cross-section is a very thin rather small cross-section, and the load was chosen to give the same displacement magnitude as in the previous section. The load with a magnitude of 160 N is applied at the secondary joint model located at the free end of the cantilever beam, where it is evenly distributed along the two web panels. Furthermore, all d.o.f. at each end-interface of the secondary joint models at the column top and bottom are fully restrained (to a clamped support condition). The remaining d.o.f. within all four joint models not being at a connected face nor assigned for load or boundary conditions are condensed. It follows that the discretisation of the joint models is mainly governed by the mesh chosen for the beam elements and is illustrated in Fig. 16. The cantilever beam cross-section is modelled using eight wall elements in each of the four walls; this results in 32 nodes at the interface and hence, 192 interface modes. The cross-section of the two advanced column elements has 16 wall elements

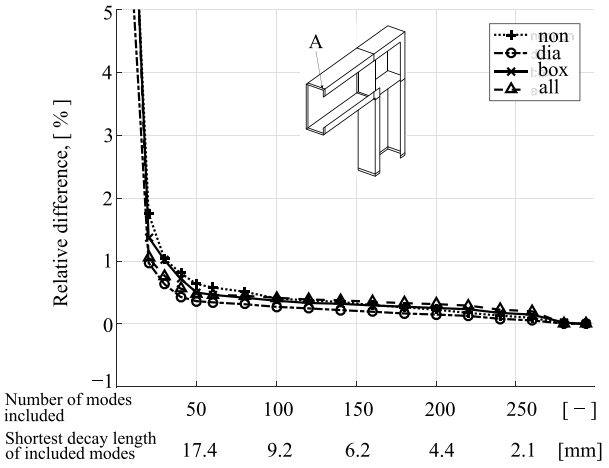

(a) The u_Z-displacements at point A

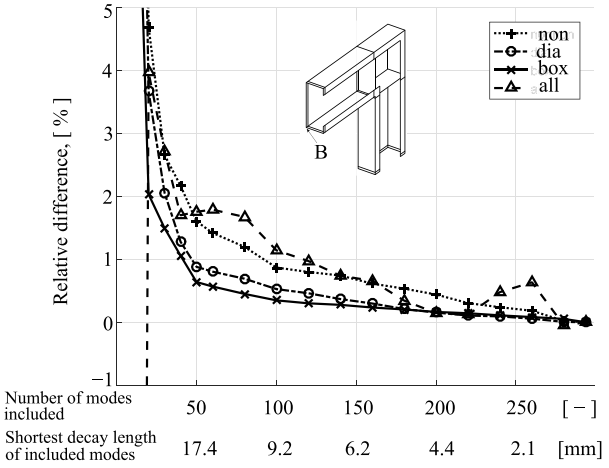

(b) The u_X-displacements at point B

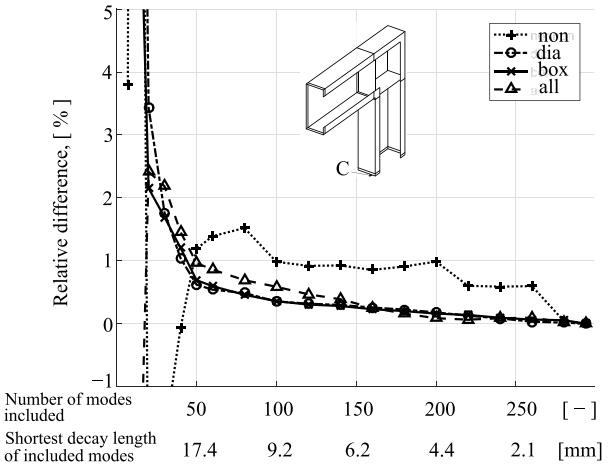

(c) The u_X-displacements at point C

Fig. 14. The influence on the displacements at point A, B and C illustrated as the relative difference when reducing the number of modes within the elements.

along the narrow sides and 12 wall elements at the wide side. This discretisation results in 56 nodes in total within a cross-section and, thus, a total of 336 interface modes at each column element interface.

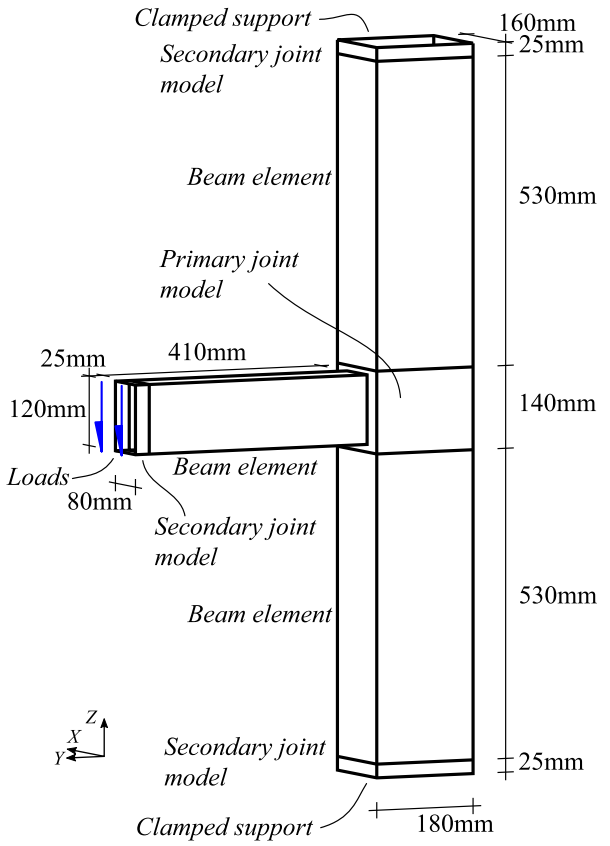

Fig. 15. Ex. 2 – The beam-to-column set up. The thickness of all plates are 2 mm.

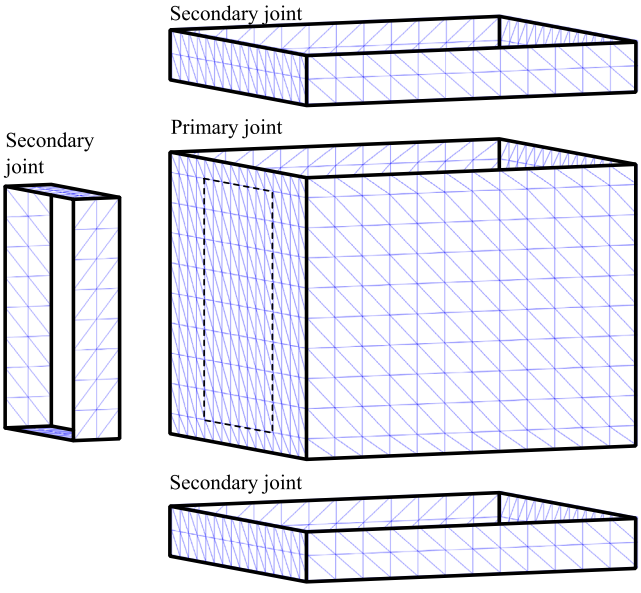

Fig. 16. Ex. 2 – Visualisation of the mesh density for the four joint models.

The discretisation of the two types of beam element cross-sections are shown in Fig. 17.

6.2.1. Ex. 2: Comparison with a finite element shell model

The vertical key point displacement at the centre of the upper flange of the cantilevered beam has been compared to that of a finite element model in Abaqus. The finite element model uses triangular shell elements (S3 elements in Abaqus nomenclature) in a structured

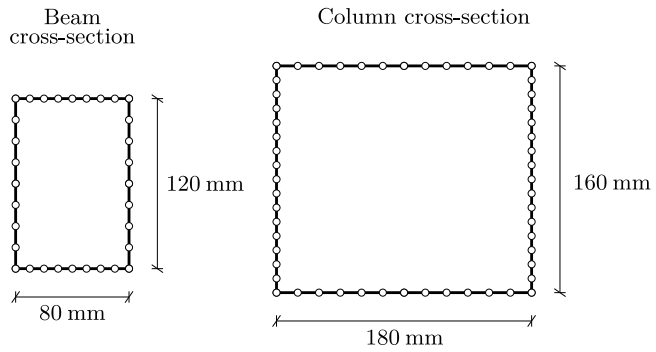

Fig. 17. Ex. 2 – Discretisation of beam and column cross-sections.

Table 4
Key point displacement at the free end of the cantilever beam for examples 2 and 3.

		Abaqus [mm]	Present method [mm]	Relative difference Δ
Example 2	u_Z	−2.026	−1.965	3.0%
Example 3	u_Z	−0.0259	−0.0282	8.9%

mesh and with full integration. The mesh is chosen such that the column cross-section has sixteen elements in each wall, whereas the beam has eight elements in the narrow flanges and sixteen elements in the webs. In general, the side length of a triangular finite element is approximately 10 mm.

The key point vertical displacement u_Z found at the free end of the cantilevered beam using the present theory and Abaqus is given in Table 4. The relative difference is found to be 3.0%. A three-dimensional comparison of the displacement magnitudes of the two models can be seen in Fig. 18. The colours indicate the total absolute magnitude of the displacements found. It can be seen how the main displacements occur at the cantilever end of the beam and that deviations between the models are magnified at the cantilever end corresponding to the key point. From Fig. 19 it can be clearly observed how local deformations are induced in the column walls in both models. For both models the displacement u_Y along the centre line of the connected column flange is plotted in Fig. 19c. It can be seen that the two models agree quite well and that the difference in the column is small and very local.

6.2.2. Ex. 2: Interface mode intensities

The beam–column structure has been analysed using the full mode space. The overall deformation of the beam–column structure is shown in Fig. 20 and a close-up of the deformation of the unequal width tubular joint is shown in Fig. 21. The mode intensities at each interface of the primary joint model are also shown on the right hand-side of Fig. 20. Due to the different discretisations of the beam and column elements, the number of interface modes at each interface is different. At Interface 1 and 3, there are 336 modes, whereas, at Interface 2, there are 192 modes. The tendency at Interface 1 and 3 is that the large intensity modes are among the first modes, and then the intensities decay for increasing mode indices. However, at Interface 2, a single mode stands out from the others, that is, mode five (rotation related to bending), and it has an intensity that is at least ten times higher than the other modes. The other modes are not decreasing, as seen at Interface 1 and 3. The first number of interface modes of Interface 2 are illustrate in Fig. 22. The magnitude of the interface mode intensities is also included in the figure. In this example, the shortest solution length scales are in the same order of magnitude as the side lengths of the triangular elements used in the joint model. Therefore an increase in mode intensities is not seen for the highest mode index values.

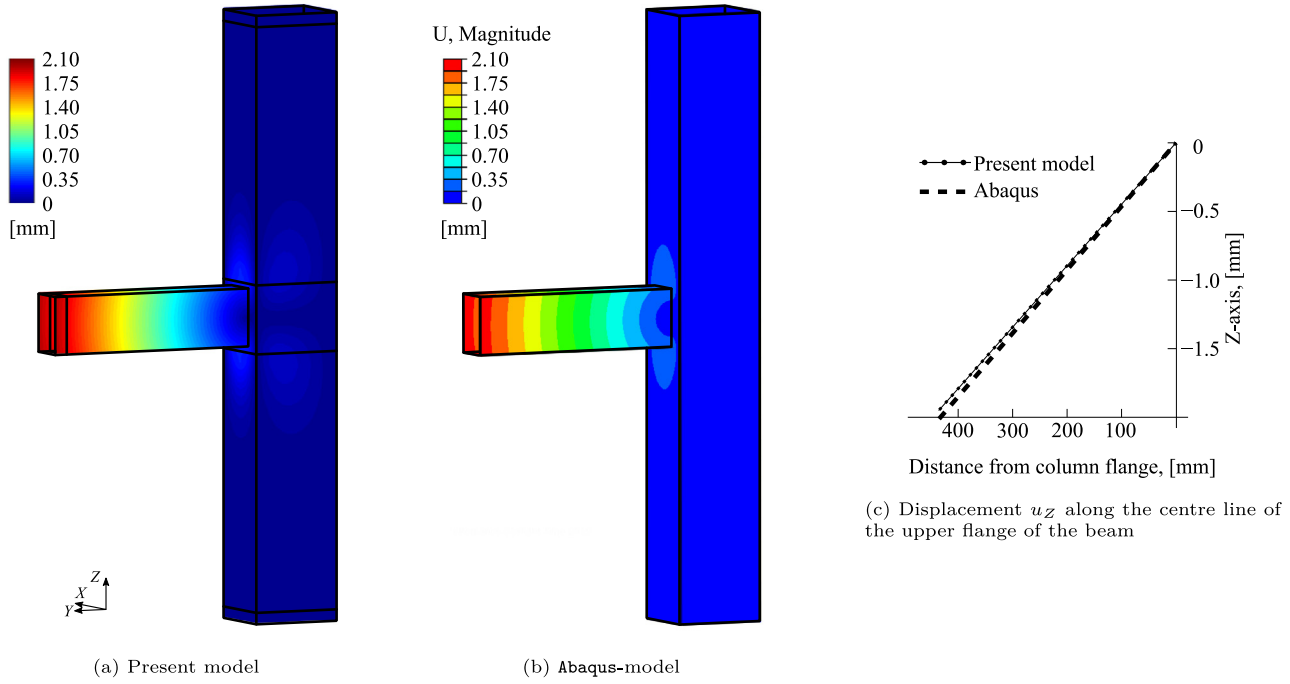

(a) Present model (b) Abaqus-model

(c) Displacement u_Z along the centre line of the upper flange of the beam

Fig. 18. Ex. 2 – Visualisation of the total absolute magnitude of the displacements in the two models.

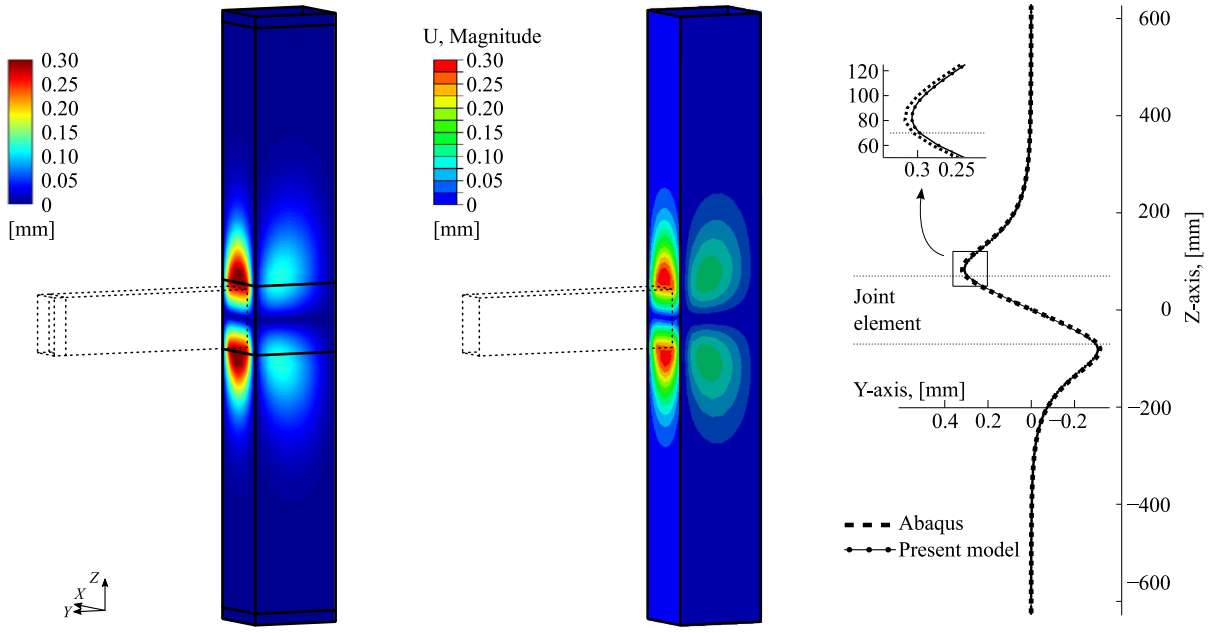

(a) Present model (b) Abaqus-model

(c) Displacement u_Y along the centre line of the connected column flange

Fig. 19. Ex. 2 – A column cut-out to visualise the absolute magnitude of the displacements in the two models.

6.2.3. Ex. 2: Interface mode reduction

Now, as in the previous example, the influence of mode reduction is investigated. The number of modes used for the analysis is decreased by twenty modes at a time until sixty modes are left, then only ten modes are removed in each step, and finally, an analysis is made with seven modes only. In line with the previous example, the Key point displacement u_Z at the cantilevered tip of the upper flange centre is found after each reduction in the number of modes. A relative difference between the key point displacement using the reduced mode space and the full mode space is computed. This allows us to make the illustration shown in Fig. 23. The thick lines correspond to this example 2. The number of modes and the decay lengths of this example is shown below the graph as lower axis labels. The relative difference in the key point displacement is also given in Table 5. It can be seen that a rapid increase in the relative difference is seen as we reduce the number of modes. The main reason for this rapid increase in the relative deviation is to be found in the way the frame joint deforms. Because the beam width does not equal the column width, the rotation that occurs at the joint is caused by local plate bending in the column walls. The interface modes related to this kind of behaviour are modes with high index numbers. Thus, the induced error will be significant if these higher-order modes are not included in the analysis. Furthermore, the main

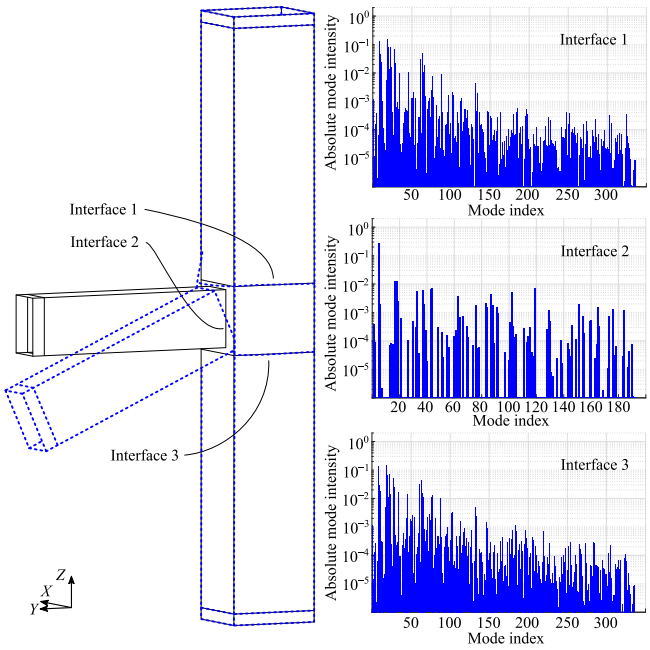

Fig. 20. Ex. 2 – Global deformation and intensities of the primary joint interfaces. The deformation is magnified by a factor of 100.

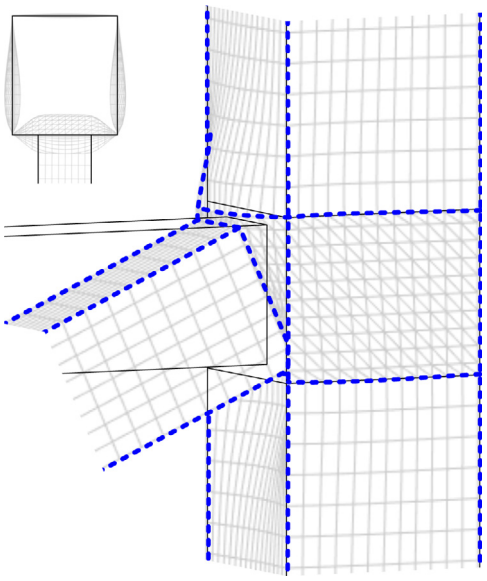

Fig. 21. Ex. 2 – A close-up of the deformation at the connection and a top view illustrating the bending of the column panels. The magnitude of the displacements are increased 100 times.

Table 5
Relative difference of beam tip displacements for interface mode reduction compared to the use of all modes.

	Tubular connection	Disp. comp	Number of included interface modes						
			200	150	100	50	20	10	7
Example 2	Unequal width	u_Z	3%	12%	21%	58%	88%	94%	99%
Example 3	Equal width	u_Z	3%	6%	7%	14%	23%	39%	44%

reason is that the stiffness of this type of connection with unequal width flanges is very limited.

6.3. Example 3 – tubular joint with equal width sections

This third academic example also investigates the effect of interface mode reduction for a connection between a cantilever tubular (RHS) beam and a tubular (RHS) column with clamped ends, as in the second example. The only change from the second example is that the geometry of the beam is now changed so that the beam flange width is equal to the column width. The changed beam cross-section and its discretisation are shown in Fig. 24. This change means that both in-plane membrane and plate bending action are now invoked to transfer the cantilever beam moment. Since the width of the beam is now greater than the height, there may still be quite a large effect from the plate bending action in transferring the flange stresses of the cantilever beam. Nevertheless, the stiffness is increased substantially. Therefore the load used is very small and leads to displacements that are magnitudes lower than example 2.

With equal width cross-sections, the key point vertical displacement at the middle of the upper flange at the free end is reduced to 1.4% of the previous example, i.e. to $u_Z = 0.028$ mm, which is a considerable reduction compared to the displacements of the second example, as seen in Table 4. The stiffness of the joint has increased substantially from second example by transferring the moment more or less directly through the side walls (webs) of the beam and column. Of course, the moment of inertia of the beam is increased since it is now twice as wide. However, the influence of the flexural bending deformation of the beam is insignificant compared to the joint deformation in these examples.

6.3.1. Ex. 3: Comparison with a finite element shell model

Table 4 shows the key point displacement of the present method and the Abaqus finite element model. It can be seen that the relative difference between this and the previous example are of the same order of magnitude.

6.3.2. Ex. 3: Interface mode intensities

Due to the changed beam width, the number of beam element modes increased from 192 in the previous example to 288 modes. Of course, the increased number of modes is due to an increased number of nodes within the beam cross-section. Nevertheless, the primary interface modes are similar and the extra modes added are modes related to a displacement with short decay lengths. With the changed beam width, the structure is analysed, and the resulting mode intensities are found. Based on analysis using the full mode space Fig. 25 shows the global deformation as well as the intensities of the modes at the interfaces similar to Fig. 20 for the original design. In accordance with the increased stiffness and the reduction in displacements, the intensities are generally decreased compared to those in Fig. 20. Note the difference in the scale of the vertical axis in the intensity plots. Since the joint invokes in-plane action in the beam and column sidewalls, it is seen that the number of high index modes having high intensities is reduced, especially at Interface 1 and 3. At Interface 2, we also see a decrease in the number of modes with a clear influence.

6.3.3. Ex. 3: Interface mode reduction

Reducing the number of interface modes as in the previous example does not as markedly increase the relative difference in the key point displacement as in the previous example. The variation in the relative difference in the key point displacement as a function of the number of included interface modes is shown in the graph of Fig. 23 for both examples. The number of modes and the decay lengths of this example is shown above the graph as top axis labels. The relative difference in the key point displacement is also given in Table 5 for both examples. From the graphs and the table, we can deduce that for equal width beam and column, the local modes with a high mode index do not

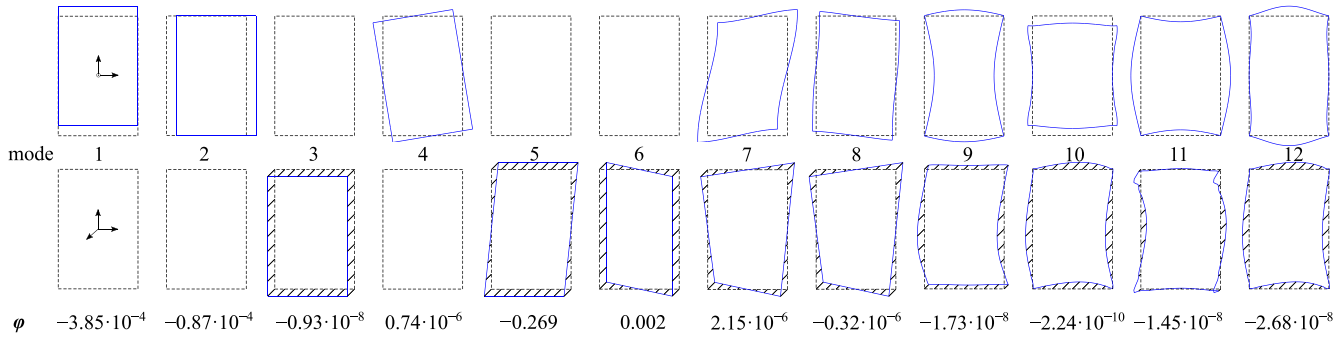

Fig. 22. Ex. 2 – The first twelve interface modes (i.e. normalised) used at Interface 2 in Fig. 20. The upper row represents the in-plane part of the displacement modes and the lower row represents the out-of-plane displacements of the modes (warping). The numbers below indicates the actual intensities of each interface mode obtained form the analysis.

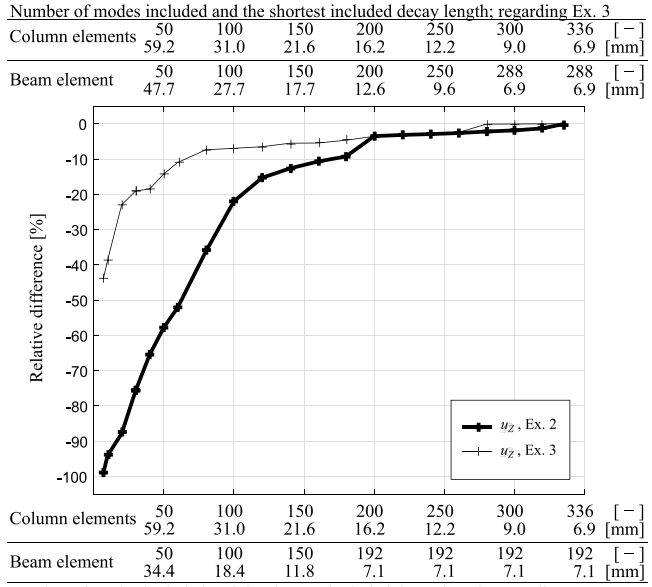

Fig. 23. Relative difference in key point displacement when reducing the number of modes within the model in examples 2 and 3.

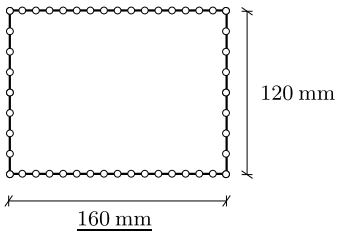

Fig. 24. Ex. 3 – Discretisation of the changed beam cross-section.

influence the displacement to the same extent as in the case with unequal widths. When keeping only the first 100 modes, the relative difference in the key point displacement is still below 8 % for equal width beam and column, whereas for the unequal widths (Ex. 2), this relative difference is 28 %. However, it is also clear that part of the moment in the cantilever beam is also transferred through plate action. In order to achieve accurate stiffness modelling, it is necessary to include local plate bending modes. Of course, if accuracy in the local stresses is important, even the full mode space may have to be included.

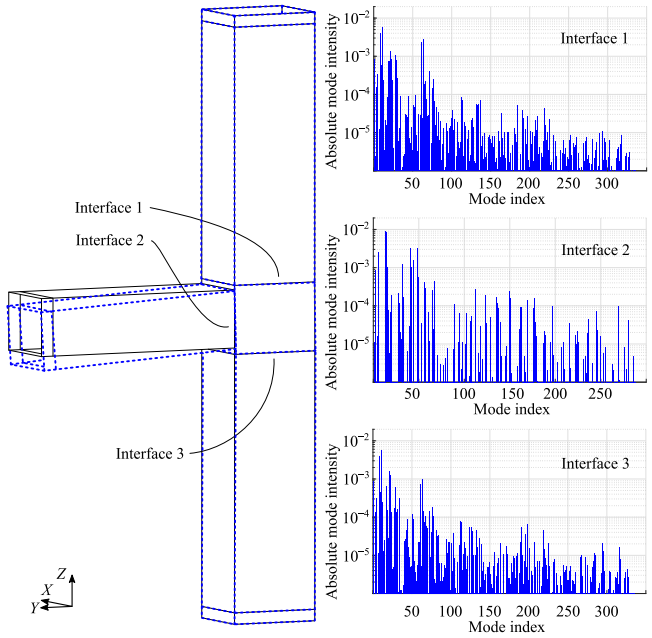

Fig. 25. Ex. 3 – Global deformation and mode intensities of the primary joint interfaces. The deformation is magnified by a factor of 1000.

6.4. Example 4 – tapered I-section joint

This fourth academic example investigates the effect of interface mode reduction for a tapered I-section joint without stiffeners. The joint example is used by Manta et al. in [13]. The joint design relies on a combination of membrane and flexural actions since the kink in the flanges is not stiffened by a third plate stiffener. The example allows a comparison of displacement results obtained by finite shell elements and by Manta et al. using GBT elements based on cubic Hermite interpolation. Two combined shell and beam models, model A and model B, shown in Fig. 26 are used for the present method. Model A is equivalent to the model used by Manta et al. with a joint extension, and model B is without the joint extensions from the end of the tapered part. Model B is used to investigate if the presented method needs an extension of the joint. The I-section geometry and the section discretisation are shown in Fig. 27, and the discretisation of the joints is shown in Fig. 28. The exponential beam modes and the related interface modes are illustrated in Fig. 29. The beam mode numbers are shown above the cross-section modes, and the interface mode numbers are shown in parenthesis. The first six interface modes corresponding to the six rigid body modes of the cross section are not included in the figure.

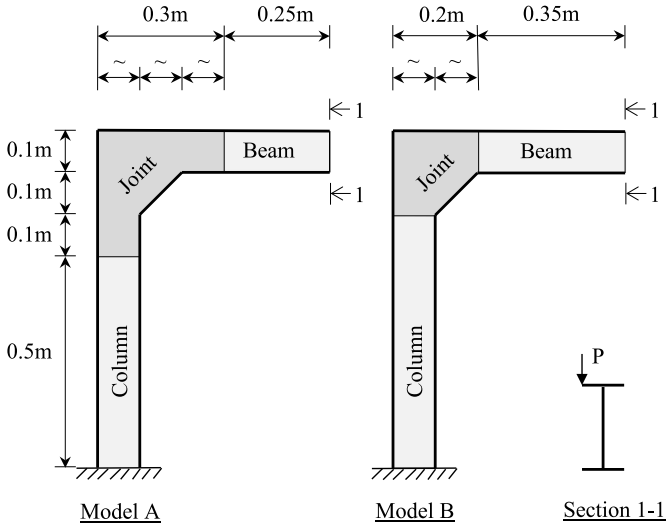

Fig. 26. Ex. 4 – Tapered I-section joint modelled with joint extension in Model A and without joint extension in Model B.

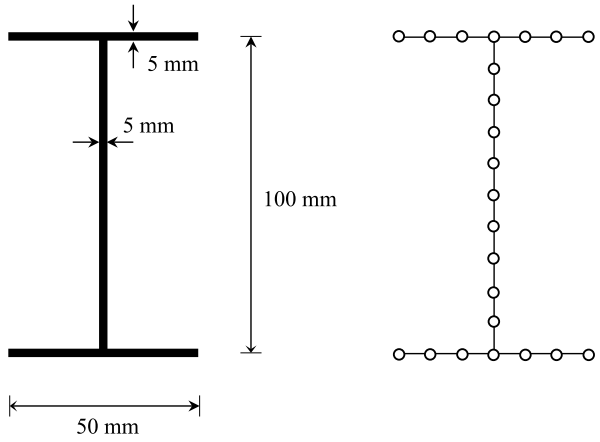

Fig. 27. Ex. 4 – Beam and column cross-section and the discretisation.

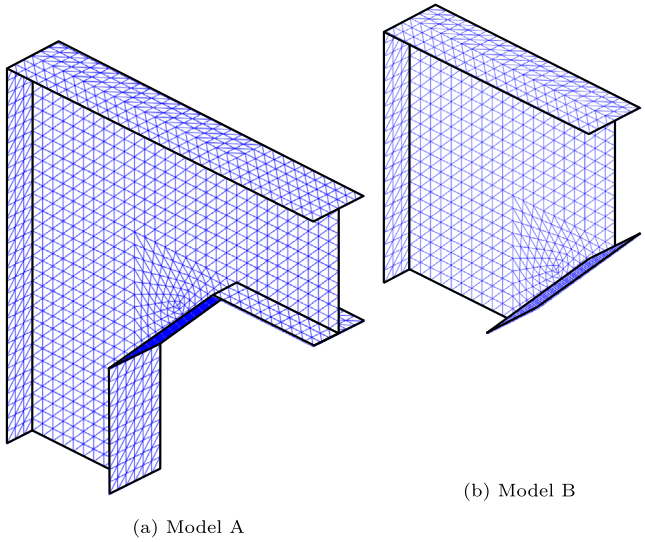

Fig. 28. Ex. 4 – Discretisation of joint models A and B.

Table 6
Ex. 4 – Key point displacement at the loaded upper flange tip of the beam. [mm].

Abaqus	Manta et al. [13]		Present method			
shell	shell	Model A	Model A		Model B	
S3	MITC4	MITC4+GBT	All modes	40 modes	All modes	40 modes
12.212	12.258	12.278	12.161	12.025	12.207	12.040

6.4.1. Ex. 4: Comparison between models

The flange tip of the cantilevered part of the beam is loaded by a transverse load of $P = 10$ kN as shown in Section 1–1 of Fig. 26. The found key point displacement of the flange tip is given in Table 6 for the different methods. The Abaqus model uses triangular S3 shell elements, with a discretisation resembling that of the cross-section, Fig. 27. The MITC4 shell model and the MITC4+GBT results are taken from [13]. For the present method, the discretisation used corresponds to all 138 modes in a cross-section. The table also includes the results in which the number of interface modes has been reduced to 40 modes. It can be seen that the results agree and that the present method does not need the extension of the connection. The beam element can handle the local deformations at the kink.

When comparing to the results of Manta et al. it has to be noted that the methods are different and the counting method for the number of modes also deviate. Therefore, the comparison has to be done by the number of d.o.f. and not by the number of modes. The present formulation of modes includes the elongation of the walls in the cross-section plane, shear deformation, and the Poisson effect. In the presented method, interface mode reduction is also strictly based on length scale. Therefore more modes are needed. Manta et al.'s results are based on Hermitian interpolation of Vlasov beam modes and five selected local plate modes. Therefore mode reduction has already been performed. Since five finite elements are used to model the column and another five to model the beam, it is estimated that the prismatic finite beam elements in Manta et al.'s model correspond to 132 d.o.f. including the end d.o.f. The full model of this paper uses 138 interface modes at each prismatic beam element end. Therefore with only one beam element in the column and one for the beam, this corresponds to $2x2x138 = 552$ d.o.f. Introducing interface mode reduction to 40 interface modes results in the use of $2x2x40 = 160$ d.o.f., which is a little higher but in the same order of magnitude as the model by Manta et al.. Furthermore, the number of d.o.f. of the shell finite element model of the prismatic beam parts (with 6 d.o.f. per node) are in the order of magnitude of 12,000 d.o.f, which is much more than the discussed advanced beam models.

6.4.2. Ex. 4: Interface mode intensities

The interface mode intensities and the deflection of the frame with the tapered I-section joint between the column and beam are shown in Fig. 30 for both models. Since the beam and column interfaces of model A are placed a section hight away from the kink, it is expected that the higher index modes have a reduced intensity compared to model B, in which the interface is placed at the kink. The following subsection shows that approximately the first 40 modes are essential for both models. From the intensity plot, it seems that more of the first 40 modes are excited in model B.

6.4.3. Ex. 4: Interface mode reduction

The influence of interface mode reduction performed as in the previous examples is illustrated in Fig. 31. The relative key point displacement difference for interface mode reduction is relative to the use of all 138 interface modes (Table 6). There is little difference between models A and B, and the number of modes can be reduced to 40 without compromising the accuracy. The relative difference values of the flange tip displacements are given in Table 7.

It can be seen that using only the six beam interface modes for this thin-walled structure leads to the 44.0–47.2% relative difference

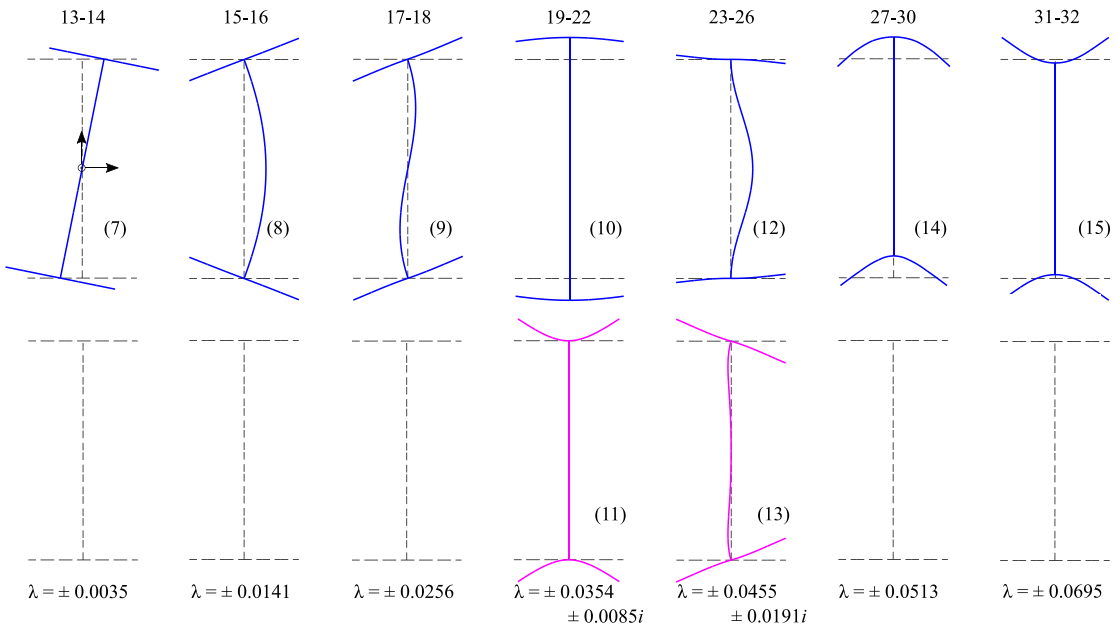

(a) The in-plane part of the I-section modes. The upper row represents the real part and the lower row represents the imaginary part of the beam modes.

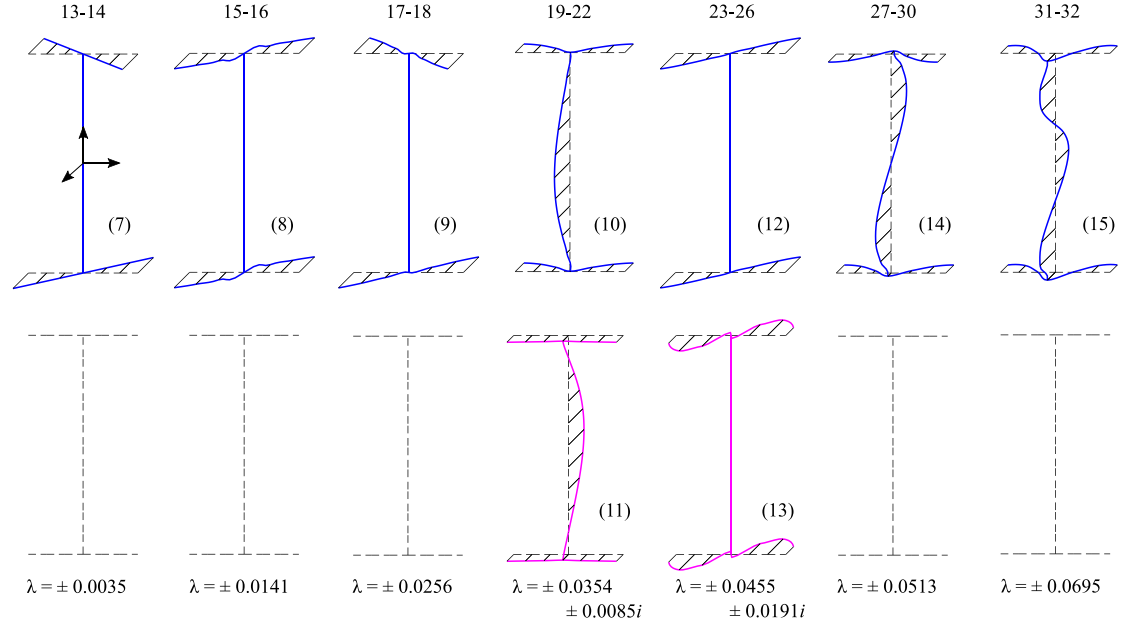

(b) The out-of-plane warping part of the I-section modes. The upper row represents the real part and the lower row represents the imaginary part of the beam modes.

Fig. 29. Ex. 4 – Exponential beam modes and the related interface modes for the I-section. The related interface mode numbers are shown in parenthesis.

Table 7
Relative difference of the flange tip displacement for interface mode reduction compared to the use of all modes.

Number of interface modes:	100	80	60	40	30	20	10	7	6
Model A	0.52%	0.65%	0.95%	1.12%	2.61%	8.13%	11.5%	14.6%	44.0%
Model B	0.55%	0.71%	1.06%	1.37%	3.17%	9.10%	13.1%	18.3%	47.2%

in the key point displacement and including the classic seventh d.o.f. reduces this to the 14.6–18.3% relative difference. Less than 2% relative difference can be obtained by including forty interface modes. The previous and this example illustrate that using standard beam elements can lead to significant displacement errors even if refined joint models are introduced.

7. Discussion

Using advanced beam elements based on the solution of the quadratic eigenvalue problem has the advantage of only introducing nodes at the end cross-sections, not having to split a beam element into finite beam elements with many nodes along the beam (as in conventional GBT beam analysis). As long as the advanced beam element

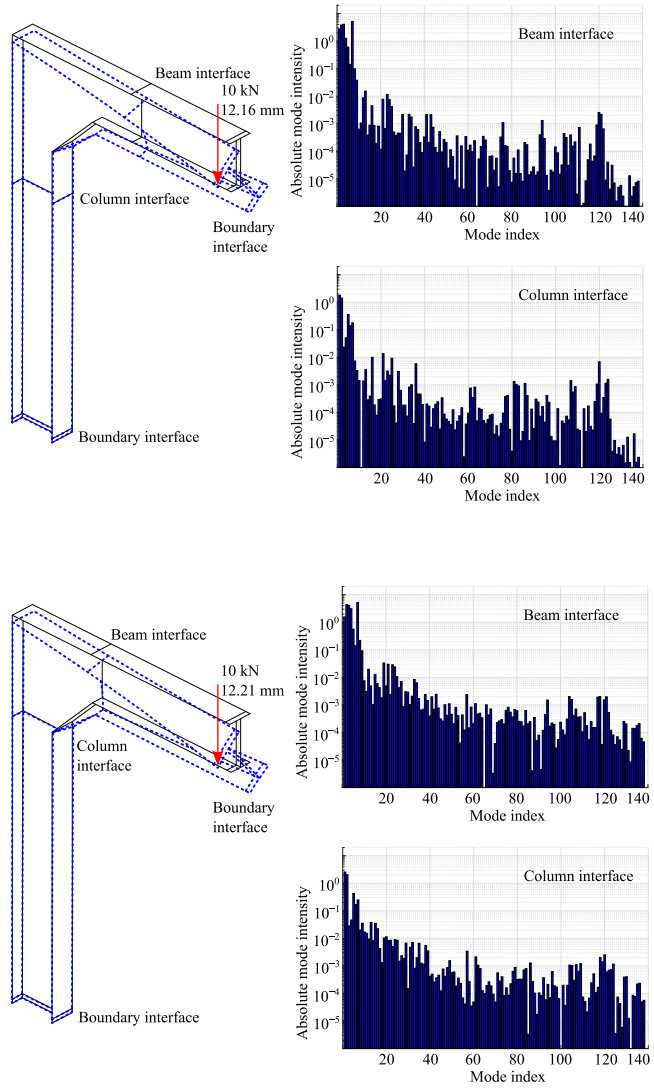

Fig. 30. Ex. 4 – Global deformation and mode intensities of the joint interfaces for model A and B. The deformation is magnified by a factor of 5.

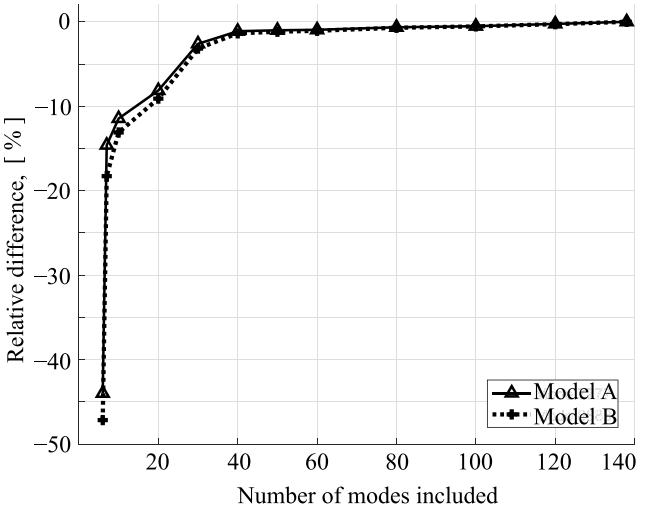

Fig. 31. Ex. 4 – Relative difference in key point displacement when reducing the number of modes used in model A and B.

is used for linear elastic analysis, the advanced beam elements will be effective. If the number of degrees of freedom at the end cross-sections can be further reduced by interface mode reduction, the number of degrees of freedom of the whole structure will be substantially reduced.

If the global modelling of larger thin-walled frame structures is to be accurate, then modelling of joint displacements and stiffnesses must be reasonably accurate. Interface mode reduction has to be applied with caution and knowledge of the connection design. Displacements and stresses converge with decreasing length scales of modes. As in displacement modelling in finite elements, stresses converge slightly slower and may need an increase in the number of included modes, especially when local plate bending effects are essential. The number of degrees of freedom needed when using advanced beam elements is much less than when using shell elements since we have utilised knowledge of the behaviour of the prismatic geometry.

In relation to the examples, it is seen from Example 1 that when the joint design is mainly based on the transfer of section forces through membrane action in the plane of the cross-section walls, then the displacement and stiffness modelling remains reasonably accurate when applying quite large interface mode reductions. However, Example 2 shows that if joints are designed based on flexural plate action, then the displacement and stiffness modelling of the joint will be compromised by interface mode reduction (the possible amount of interface mode reduction will be relatively insignificant). On the other hand, Example 3 shows that as soon as just some of the cross section walls are allowed to transfer forces through in-plane action to the joint, the interface mode reduction may be applied to a reasonable level. In these examples, we have only focused on a direct connection of the beams to the joint. These direct connection interfaces can be achieved by welding. We are aware that many possible connection designs may be appropriate and that there is a need for further investigation.

Including modes according to decreasing length scales (equivalent to ascending order of eigenvalues) is a natural systematic choice corresponding to increasing the discretisation in finite element analysis or increasing the number of Fourier terms in series approximations. The shorter the length scales included are, the more refined the approximation will be. Including modes of short length scale by an informed engineering choice will often only lead to appropriate approximations if most of the modes with larger length scales are also included.

Using beam modes as interface modes are justified by the axial displacement part of the beam modes (flexural, torsional and distortional warping modes) being very stiff (in the plane of the cross-section walls) and therefore often inducing the related displacements to the joint or transferring the related axial stresses to the joint. However, if the joint does not resist through in-plane membrane action, then local transverse (out of plane) plate action occurs in both beam element and joint model. As shown, interface mode reduction may be difficult using the present method. Of course, this will depend on the thickness of the plates used in the joint.

The decay length of the essential beam modes is important in relation to the discretisation and modelling of the joint, since the shell element discretisation has to accommodate these decay lengths within the joint. Thus, using the decay length as a predictor for the number of interface modes at the joint has relevance.

Compared to the level of accuracy obtained using standard frame analysis without including joint flexibility, the presented method gives a proposal that can be used to successively refine the accuracy of global frame analysis by including an increasing number of modes. However, the accuracy is dependent on an appropriate joint design.

8. Conclusion

This paper has introduced a mode selection technique that leads to a unique set of interface modes, for the GBT methods based on solution of the related quadratic eigenvalue problem. Furthermore, ordering the modes by length scales (eigenvalues) gives a natural choice of mode

reduction by reducing the number of modes from the small length scale end. This paper shows how interface mode reduction can substantially reduce the number of degrees of freedom by using beam interface modes. It has also been found that mode interface reduction has to be applied with caution and due consideration of the joints at which it is applied. Membrane transfer of forces allows a higher degree of mode interface reduction.

Declaration of competing interest

The authors declare that they have no known competing financial interests or personal relationships that could have appeared to influence the work reported in this paper.

Acknowledgements

The first two authors thankfully acknowledge the financial support given by the Danish consultancy company NIRAS A/S and the Innovation Fund Denmark (grant 5189-00005B).

The first author appreciates the supervision given by Associate Professor Ricardo F. Vieira during two-month research stay at the Technical University of Lisbon in 2018.

A special thanks shall also be addressed to Associate Professor Michael Andreassen and Senior Specialist, Ph.D. Thomas Hansen from the Technical University of Denmark and NIRAS A/S, respectively. They have both contributed to this paper through academic discussions.

References

[1] A.B. Hansen, J. Jönsson, Modelling of steel frames using advanced beam and joint elements with interfaces governed by beam modes, Thin-Walled Struct. (2019) http://dx.doi.org/10.1016/j.tws.2019.106430.

[2] A.B. Hansen, J. Jönsson, Displacement modes of a thin-walled beam model with deformable cross sections, Thin-Walled Struct. 141 (2019) 576–592, http://dx.doi.org/10.1016/j.tws.2019.01.052.

[3] A.B. Hansen, J. Jönsson, A thin-walled beam element based on semi-analytical solution modes, Thin-Walled Struct. 144 (2019) http://dx.doi.org/10.1016/j.tws.2019.106344.

[4] R. Schardt, Verallgemeinerte Technische Biegetheorie - Band 1, Lineare Theorie, second ed., Metrum-Verlag, Darmstadt, 1989.

[5] N. Silvestre, D. Camotim, First-order generalised beam theory for arbitrary orthotropic materials, Thin-Walled Struct. 40 (2002) 755–789, http://dx.doi.org/10.1016/S0263-8231(02)00025-3.

[6] M. Abambres, D. Camotim, N. Silvestre, K.J.R. Rasmussen, GBT-based structural analysis of elastic-plastic thin-walled members, Comput. Struct. 136 (2014) 1–23, http://dx.doi.org/10.1016/j.compstruc.2014.01.001.

[7] C. Basaglia, D. Camotim, N. Silvestre, GBT-Based global buckling analysis of plane and space thin-walled steel frames, in: Proceedings of the International Collquium on Stability and Ductility of Steel Structures, SDSS 2006, IST Press, 2006, pp. 381–388.

[8] C. Basaglia, D. Camotim, N. Silvestre, Global buckling analysis of plane and space thin-walled frames in the context of GBT, Thin-Walled Struct. 46 (2008) 79–101, http://dx.doi.org/10.1016/j.tws.2007.07.007.

[9] C. Basaglia, D. Camotim, N. Silvestre, GBT-Based local, distortional and global buckling analysis of thin-walled steel frames, Thin-Walled Struct. 47 (2009) 1246–1264, http://dx.doi.org/10.1016/j.tws.2009.04.003.

[10] C. Basaglia, D. Camotim, N. Silvestre, GBT-Based buckling analysis of thin-walled steel frames with arbitrary load and support conditions, Int. J. Struct. Stab. Dyn. 10 (3) (2010) 363–385, http://dx.doi.org/10.1142/S021945510003531.

[11] D. Camotim, C. Basaglia, N. Silvestre, GBT Buckling analysis of thin-walled steel frames: A state-of-the-are-report, Thin-Walled Struct. 48 (2010) 726–743, http://dx.doi.org/10.1016/j.tws.2009.12.003.

[12] M.J. Bianco, Coupling between Shell and Generalized Beam Theory (GBT) elements (Ph.D. thesis), Bauhaus-University Weimar, Faculty of Civil Engineering, 2019.

[13] D. Manta, R. Gonçalves, D. Camotim, Combining shell and GBT-based finite elements: Linear and bifurcation analysis, Thin-Walled Struct. 152 (2020) http://dx.doi.org/10.1016/j.tws.2019.106665.

[14] D. Manta, R. Gonçalves, D. Camotim, Combining shell and GBT-based finite elements: Plastic analysis with adaptive mesh refinement, Thin-Walled Struct. 158 (2021) http://dx.doi.org/10.1016/j.tws.2020.107205.

[15] D. Manta, R. Gonçalves, D. Camotim, On the combination of shell and GBT-based beam finite elements, in: Website Proceedings of Structural Stability Research Council (SSRC) Annual Stability Conference, Louisville (Virtual), 2021.

[16] D. Manta, R. Gonçalves, D. Camotim, Combining shell and GBT-based finite elements: Vibration and dynamic analysis, Thin-Walled Struct. 167 (2021) http://dx.doi.org/10.1016/j.tws.2021.108187.

[17] R.F. Vieira, F.B.E. Virtuoso, E.B.R. Pereira, A higher order thin-walled model including warping and shear modes, Int. J. Mech. Sci. 66 (2013) 67–82, http://dx.doi.org/10.1016/j.ijmecsci.2012.10.009.

[18] R.F. Vieira, F.B. Virtuoso, E.B.R. Pereira, A higher order model for thin-walled structures with deformable cross-sections, Int. J. Solids Struct. 51 (2014) 575–598, http://dx.doi.org/10.1016/j.ijsolstr.2013.10.023.

[19] R.D. Cook, D.S. Malkus, M.E. Plesha, Concepts and Applications of Finite Element Analysis, third ed., John Wiley & Son, NewYork Chichester Brisbane Toronto Singapore, 1989.

[20] B. Specht, Modified shape functions for the three-node plate bending element passing the patch test, Internat. J. Numer. Methods Engrg. 26 (1988) 705–715, http://dx.doi.org/10.1002/nme.1620260313.

[21] A.B. Hansen, J. Jönsson, A GBT-Framework Towards Modal Modelling of Steel Structures, Vol. 1, John Wiley & Sons, Ltd – Ce/Papers, 2017, pp. 1822–1830, http://dx.doi.org/10.1002/cepa.226.

[22] G. Strang, Introduction To Linear Algebra, Wellesley-Cambridge Press, 2009.

[23] R.F. Vieira, A Higher Order Thin-Walled Beam Model (Ph.D. thesis), Universidade Técnica de Lisboa - Instituto Superior Técnico, 2010.

[24] M. Morandini, M. Chierichetti, P. Mantegazza, Characteristic behavior of prismatic anisotropic beam via generalized eigenvectors, Int. J. Solids Struct. 47 (2010) 1327–1337, http://dx.doi.org/10.1016/j.ijsolstr.2010.01.017.

[25] F. coise Tisseur, K. Meerbergen, The quadratic eigenvalue problem, Soc. Ind. Appl. Math. 43 (2) (2001) 235–286, doi:10.1.1.32.9042.

[26] J. Jönsson, Distortional theory of thin-walled beams, Thin-Walled Struct. 33 (1999) 269–303, http://dx.doi.org/10.1016/S0263-8231(98)00050-0.

[27] Matlab, Matlab® and Simulink® Used for Technical Computing, 2016, Matlab - ′ 1984-2016 The MathWorks, Inc., Version 2016a.

[28] Abaqus, Abaqus/CAE 2016; Abaqus® and SIMULIA® Used for Finite Element Analysis, 2016, Abaqus Inc., SIMULIA ′ Dassault Systèmes, 2015, Version 2016.

[29] V.Z. Vlasov, Thin-Walled Elastic Beams, second ed., Jerusalem, 1961, Israel Program for scientific translations.